



RESEARCH ARTICLE

10.1029/2021MS002620

Improved Quantification of Ocean Carbon Uptake by Using Machine Learning to Merge Global Models and pCO₂ Data

L. Gloege^{1,2} , M. Yan³, T. Zheng^{3,4} , and G. A. McKinley¹ 

¹Lamont-Doherty Earth Observatory and Department of Earth and Environmental Sciences, Columbia University, New York, NY, USA, ²Now at NASA-GISS, New York, NY, USA, ³Department of Statistics, Columbia University, New York, NY, USA, ⁴Data Science Institute, Columbia University, New York, NY, USA

Special Section:

Machine learning application to Earth system modeling

Key Points:

- With models as a prior to be corrected by partial pressure of CO₂ (pCO₂) data, LDEO-HPD uses machine learning to estimate global ocean monthly pCO₂ for 1982–2018
- Lamont Doherty Earth Observatory-Hybrid Physics Data (LDEO-HPD) agrees better with independent pCO₂ data than other currently available products
- LDEO-HPD can be used as a diagnostic tool to evaluate spatio-temporal model fields

Correspondence to:

L. Gloege,
ljpg2157@columbia.edu

Citation:

Gloege, L., Yan, M., Zheng, T., & McKinley, G. A. (2022). Improved quantification of ocean carbon uptake by using machine learning to merge global models and pCO₂ data. *Journal of Advances in Modeling Earth Systems*, 14, e2021MS002620. <https://doi.org/10.1029/2021MS002620>

Received 17 MAY 2021

Accepted 30 DEC 2021

Author Contributions:

Conceptualization: L. Gloege, M. Yan, T. Zheng, G. A. McKinley
Data curation: L. Gloege
Formal analysis: L. Gloege, M. Yan
Funding acquisition: G. A. McKinley
Investigation: L. Gloege, M. Yan
Methodology: L. Gloege, M. Yan, T. Zheng, G. A. McKinley
Project Administration: G. A. McKinley

© 2022 The Authors. *Journal of Advances in Modeling Earth Systems* published by Wiley Periodicals LLC on behalf of American Geophysical Union. This is an open access article under the terms of the [Creative Commons Attribution-NonCommercial License](https://creativecommons.org/licenses/by/4.0/), which permits use, distribution and reproduction in any medium, provided the original work is properly cited and is not used for commercial purposes.

Abstract The ocean plays a critical role in modulating climate change by sequestering CO₂ from the atmosphere. Quantifying the CO₂ flux across the air-sea interface requires time-dependent maps of surface ocean partial pressure of CO₂ (pCO₂), which can be estimated using global ocean biogeochemical models (GOBMs) and observational-based data products. GOBMs are internally consistent, mechanistic representations of the ocean circulation and carbon cycle, and have long been the standard for making spatio-temporally resolved estimates of air-sea CO₂ fluxes. However, there are concerns about the fidelity of GOBM flux estimates. Observation-based products have the strength of being data-based, but the underlying data are sparse and require significant extrapolation to create global full-coverage flux estimates. The Lamont Doherty Earth Observatory-Hybrid Physics Data (LDEO-HPD) pCO₂ product is a new approach to estimating the temporal evolution of surface ocean pCO₂ and air-sea CO₂ exchange. LDEO-HPD uses machine learning to merge high-quality observations with state-of-the-art GOBMs. We train an eXtreme Gradient Boosting (XGB) algorithm to learn a non-linear relationship between model-data mismatch and observed predictors. GOBM fields are then corrected with the predicted model-data misfit to estimate real-world pCO₂ for 1982–2018. The resulting reconstruction by LDEO-HPD is in better agreement with independent pCO₂ observations than other currently available observation-based products. Within uncertainties, LDEO-HPD global ocean uptake of CO₂ agrees with other products and the Global Carbon Budget 2020.

Plain Language Summary The ocean absorbs carbon from the atmosphere, which slows climate change. In order to estimate how much carbon the ocean absorbs, we need to know how much is exchanged from the atmosphere into the ocean at each location over time. The direct observations required to do this are very sparse and in some regions of the ocean, observations have never been made. One approach to fill in the gaps is to use machine-learning techniques, which are algorithms that build a relationship for ocean carbon based on related satellite observations with global coverage. Another approach is to use computer simulations, which use mathematical equations to represent ocean processes. Here, we merge these two innovations by blending model output with machine-learning to create a hybrid product: the Lamont Doherty Earth Observatory-Hybrid Physics Data (LDEO-HPD). Particularly for the most recent decade, LDEO-HPD agrees better with independent observations than other products, indicating promise for the approach.

1. Introduction

The ocean's net uptake of CO₂ is a key component of the global carbon cycle. Quantifying how anthropogenic emissions are distributed between atmosphere, land biosphere, and ocean reservoirs with as low uncertainty as possible is needed to support international climate policy (Peters et al., 2017). The Global Carbon Budget 2020 (Friedlingstein et al., 2020) finds that for 2009–2018, the ocean sink for anthropogenic carbon was -2.5 ± 0.6 PgC/yr (negative flux into the ocean), based on global ocean biogeochemical models (GOBMs). However, four observation-based products suggest a trend diverging from the GOBMs over this period and a sink that is 0.4 PgC/yr larger (Hauck et al., 2020). Do the relatively new observation-based estimates indicate an issue with the long-used GOBMs?

Estimating the global ocean CO₂ sink requires knowledge of ocean partial pressure of CO₂ (pCO₂). The Surface Ocean CO₂ Atlas (SOCAT) is an annually compiled database of surface ocean fugacity of CO₂ (fCO₂) with over 28.2 million observations for 1957–2019 in the SOCATv2020 release (Bakker et al., 2016), mainly from volunteer observing ships. fCO₂ is nearly equivalent to pCO₂, different by a 0.3% non-ideality correction; we make

Resources: L. Gloege, G. A. McKinley
Software: L. Gloege, M. Yan
Supervision: T. Zheng, G. A. McKinley
Validation: L. Gloege
Visualization: L. Gloege
Writing – original draft: L. Gloege, G. A. McKinley
Writing – review & editing: L. Gloege, M. Yan, T. Zheng, G. A. McKinley

this adjustment in our analysis to derive $p\text{CO}_2$ (Section 2.1). Due to limited number of ships, routes, and the high cost of maintenance, the data retrieved from this observation system remains sparse in space and time. Data are concentrated in the Northern Hemisphere (Figures 1a–b1c). Using these data alone, $p\text{CO}_2$ cannot be quantified at all times and all locations, and thus statistical extrapolations have been performed to create observation-based data products (Rödenbeck et al., 2015). The carbon cycle community uses these products along with GOBMs (Friedlingstein et al., 2020) to independently estimate CO_2 fluxes and, through their analysis and comparison, to improve knowledge of the global ocean carbon cycle. We propose an explicit merging of the strengths of both approaches in the form of a hybrid observation-based data product that uses $p\text{CO}_2$ estimates from multiple GOBMs as a prior.

A GOBM is a knowledge-based model that parameterizes the physical, chemical, and biological processes influencing surface ocean $p\text{CO}_2$ using a system of coupled differential equations. GOBMs have long been taken as the best estimate of the anthropogenic air-sea CO_2 flux, and have always been the basis for quantification of the ocean carbon sink in the annual Global Carbon Budget published by the Global Carbon Project since 2009 (Friedlingstein et al., 2020; Le Quéré et al., 2009). Nine GOBMs were used as the basis for the Global Carbon Budget in 2019 and 2020 (Friedlingstein et al., 2019, 2020). These models are certainly imperfect, with substantial differences among them and potentially an underestimation of CO_2 flux variability, particularly in the Southern Ocean (Gloege et al., 2021; Gruber, Landschützer, et al., 2019; Hauck et al., 2020). Regional mean flux biases can also be substantial (Fay & McKinley, 2021). However, based on a long history of their application to understanding and quantification of air-sea CO_2 fluxes, it is a sensible to use GOBMs as a prior estimate upon which data-based improvements can be made.

Most observation-based products find a relationship between a suite of datasets and the target variable (ocean $p\text{CO}_2$) using machine learning algorithms. The statistical relationships of the algorithm are dependent on the quantity and quality of SOCAT $p\text{CO}_2$ data, driver data, and the skill of the reconstruction algorithm. A recent assessment of the SOM-FFN (Landschützer et al., 2014) reconstruction indicates high fidelity for the mean and seasonality of $p\text{CO}_2$ -based CO_2 flux estimates. However, $p\text{CO}_2$ data sparsity (Figures 1a–b1c) limits the ability to reconstruct interannual to decadal timescale variations (Gloege et al., 2021). Though the spread across the full suite of recently published products is smaller than the spread across the current generation of models (McKinley et al., 2020), there remain substantial differences in the timing and amplitude of interannual variability (Friedlingstein et al., 2020). In a comprehensive evaluation of multiple products, Gregor et al. (2019) find comparable skill with respect to independent data in the current generation of products, and suggest that we have reached a skill limit for these products that is fundamentally due to data sparsity.

Both GOBMs (Friedlingstein et al., 2020; Hauck et al., 2020) and observation-based products (Rödenbeck et al., 2015) provide approximately global estimates of ocean $p\text{CO}_2$ and CO_2 flux. The two approaches differ significantly in the way they estimate ocean $p\text{CO}_2$. GOBMs compute the evolution of physical and biogeochemical processes based on complex systems of coupled differential equations that can only be solved numerically. Observation-based products do not explicitly incorporate known physics, but instead estimate a non-linear relationship between a suite of driver variables (e.g., see Table 2) and ocean $p\text{CO}_2$ where these are co-located. Global full-coverage driver datasets are then processed through these relationships to estimate global full-coverage $p\text{CO}_2$. GOBMs and observation-based data products generally agree on the large-scale patterns and long-term increase in ocean $p\text{CO}_2$ (Landschützer et al., 2014; McKinley et al., 2016, 2020; Tjiputra et al., 2014). GOBMs have comparable root mean square errors against SOCAT $p\text{CO}_2$ to those in the observation-based products when compared over large spatial regions, indicating comparable skill (Gregor et al., 2019; Hauck et al., 2020). However, GOBMs are biased high when sub-sampled at SOCAT observation locations (Figure 1d). In some models, this global bias is at least partially attributable to the exclusion of the well-established water vapor correction (Dickson et al., 2007) in the calculation of atmospheric $p\text{CO}_2$ (McKinley et al., 2020).

As noted above, the $p\text{CO}_2$ data typically available to train machine learning algorithms are spatially sparse (Figures 1a–b1c). Data availability also changes over time (Figures 2a and 2b). This trend in data availability, combined with the long-term positive trend in ocean $p\text{CO}_2$ ($\sim 33 \mu\text{atm}$ increase from 1980s to 2010s) has the potential to impact the ability of algorithms to represent the data. Machine learning, or any statistical fit, performs best when target variables distributions have the same shape as the driver variables (Goodfellow et al., 2016). With ocean $p\text{CO}_2$ as the target variable, the algorithm is being asked to predict a broad and right-skewed distribution (Figure 2a) that is unlike the driver variables that do not have a significant trend across time. For other products,

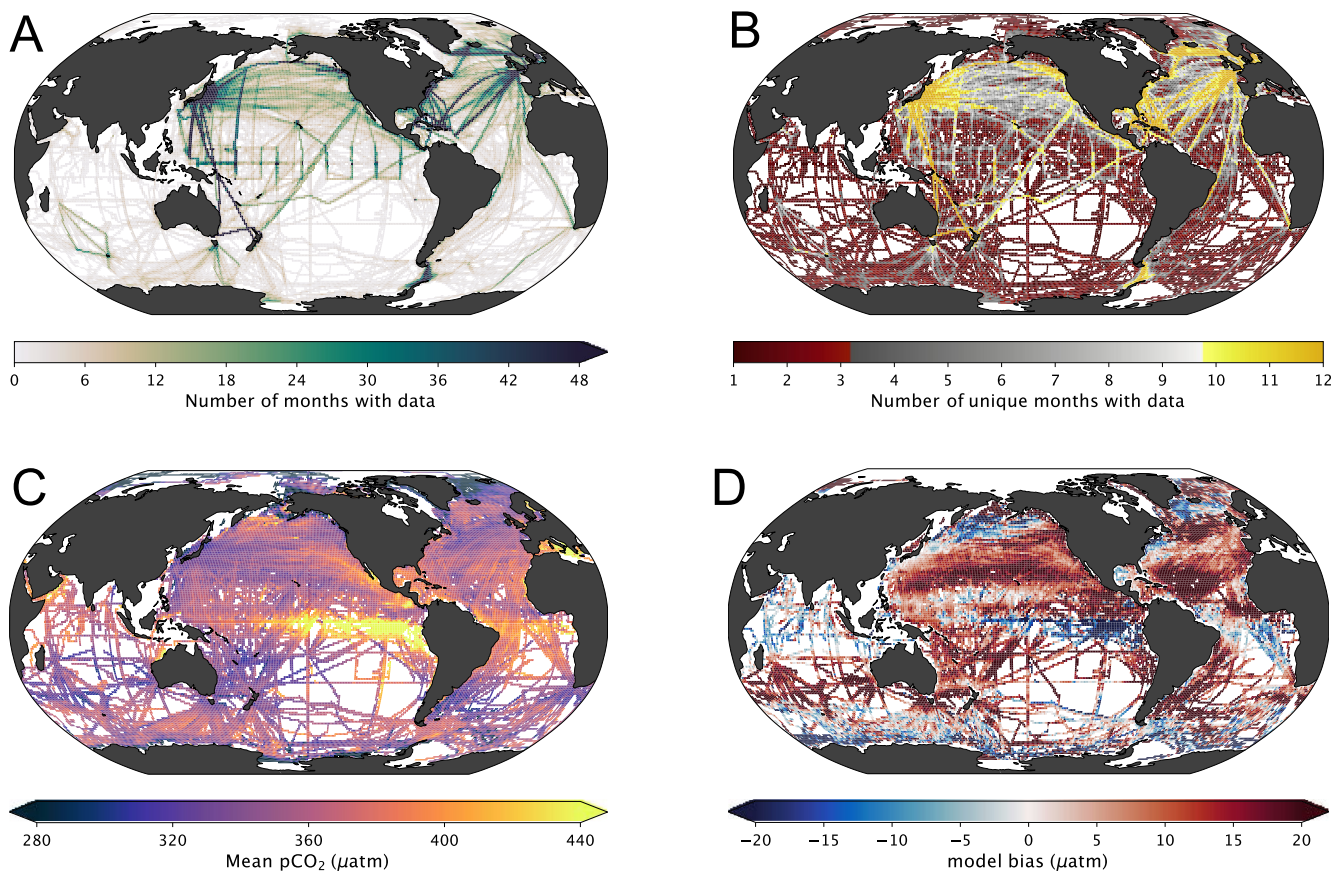


Figure 1. (a) Total number of months over 1982–2018 with observations. (b) Number of unique months with observations. (c) Long-term mean pCO₂ at each 1° × 1° pixel. (d) Bias between Surface Ocean CO₂ Atlas and mean of nine global ocean biogeochemical models.

the temporal trend of pCO₂ is addressed by including atmospheric pCO₂ as a predictor variable. We note that the difference between observed and GOBM-estimated pCO₂ has only a modest long-term trend (~9 μatm from 1980s to 2010s, Figures 2c and 2d). Thus, if we use the difference between SOCAT observations and the GOBMs as a basis for algorithm development, we largely address the aforementioned concern. In other words, with model-data misfit as our target variable, the skewness of the target variable is substantially reduced (Figure 2c).

In this study, we leverage the nine GOBMs used in the Global Carbon Budget 2020 (Friedlingstein et al., 2020) and combine them with a supervised machine learning algorithm to create the Lamont Doherty Earth Observatory-Hybrid Physics Data ocean pCO₂ observation-based product (LDEO-HPD). Instead of using ocean pCO₂ as the target variable, as do other data products (Denvil-Sommer et al., 2019; Gregor et al., 2019; Landschützer et al., 2014; Rödenbeck et al., 2015), the target variable for our eXtreme Gradient Boosting (XGB) algorithm is the misfit between SOCAT observed pCO₂ and each model where SOCAT observations exist in space and time (pCO_{2,SOCAT} - pCO_{2,GOBM}). Our driver data are the same suite of in situ and satellite observations used by other approaches (see Table 2). To make final estimates of actual ocean pCO₂, the XGB algorithm first uses full-field observed driver data to predict model misfit at all locations for each GOBM. These misfit fields are then added back to each GOBM to make the final estimate. Each GOBM is processed using a unique algorithm, and the final LDEO-HPD output is the average of the nine merged data-model estimates. See Figure 3 for a schematic. Our approach of combining data-based machine learning with the physics embodied in dynamical models follows on recent innovations in physics-guided machine learning (Karpatne et al., 2017; Reichstein et al., 2019) and the use of machine learning to correct dynamical models (Watt-Meyer et al., 2021) for earth science applications.

A potential additional application of the approach we develop here is to use model-data misfit fields to visualize and quantify errors in GOBM carbon cycle simulations at broader temporal and spatial scales than is currently possible with actual SOCAT data (Hauck et al., 2020). Spatio-temporal misfit mapped by the algorithm is a direct

Table 1

Reference for GOBMs Used in the Global Carbon Budget 2020 (Friedlingstein et al., 2020)

Global ocean biogeochemical models (GOBMs)	Reference
NEMO-PlankTOM5	Buitenhuis et al. (2013)
MICOM-HAMOCC (NorESM1-OCv1.2)	Schwinger et al. (2016)
MPIOM-HAMOCC6 (MPI)	Paulsen et al. (2017)
NEMO3.6-PISCESv2-gas (CNRM)	Berthet et al. (2019)
CISRO	Law et al. (2017)
FESCOM-1.4-REcoM2	Hauck et al. (2020)
MOM6-COBALT (princeton)	Adcroft et al. (2019)
CESCM-ETHZ	Doney et al. (2009)
NEMO-PISCES (IPSL)	Aumont et al. (2015)

estimate of GOBM skill for locations where in situ data do not exist. We briefly explore this application in Section 3.1.

2. Methods

GOBM output is incorporated into a supervised machine learning algorithm to create a hybrid data product for 1982–2018. We use gradient boosting as implemented in the XGB library (Chen & Guestrin, 2016). XGB learns a non-linear relationship between a suite of features and the misfit between the GOBM and direct SOCAT observations. We use this approach to upscale SOCAT pCO₂ observations and create a nearly global, temporally complete data product. The upscaled pCO₂ product is statistically evaluated against independent observations and other published data products. A schematic of LDEO-HPD is shown in Figure 3. From pCO₂ estimated with LDEO-HPD, we estimate CO₂ flux using the standard bulk parameterization that relates the flux to wind speed (Fay et al., 2021; Wanninkhof, 1992, 2014).

2.1. Pre-Processing SOCAT Observations

We use surface ocean pCO₂ calculated from the SOCAT v2019 monthly gridded fCO₂ product. SOCAT v2019 is a quality-controlled data set that contains observations of surface ocean fCO₂, which is converted to pCO₂ with Equation 1,

$$pCO_2 = fCO_2 \cdot \exp\left(P_{atm}^{surf} \cdot \frac{B + 2\delta}{R \cdot T}\right)^{-1} \quad (1)$$

where P_{atm}^{surf} is the atmospheric surface pressure from ECMWF Reanalysis version 5, T is the sea surface temperature (SST) in Kelvin from National Oceanic and Atmospheric Administration (NOAA) optimally interpolated SST version 2 (OISSTv2), B and δ are virial coefficients from Weiss (1974), R is the gas constant (Dickson et al., 2007).

2.2. Global Ocean Biogeochemical Models

As a first guess for ocean pCO₂, we use output from nine GOBMs (Table 1) which participated in the Global Carbon Budget 2020 (Friedlingstein et al., 2020), with the final year being 2018. Meteorological reanalysis and atmospheric CO₂ are used to force each model (Hauck et al., 2020). Each GOBM parameterizes the physical, chemical, and biological processes influencing surface ocean pCO₂ using a system of coupled differential equations. The surface pCO₂ from each GOBM is bi-linearly interpolated from the native model grid to a 1° × 1° monthly resolution to be consistent with SOCAT gridded observations (Sabine et al., 2013).

2.3. Machine Learning Method and the LDEO-HPD Product

XGB (Chen & Guestrin, 2016) is a supervised machine learning algorithm where multiple features, X , are used to predict a target variable y . The XGB algorithm can then be used to estimate a function, $f(X)$, such that: $y \approx f(X)$. The algorithm begins with an initial guess for y , a choice to which the algorithm is not sensitive. As illustrated in Figure 3b, a decision tree is used to learn the difference between the training data and the initial guess. This new tree is added to the initial guess. This process of adding trees to correct the errors made in the summation of previous trees is repeated until either a predefined number of trees has been made, or when adding an additional tree results in no further improvement. Improvements are marginal if there are more than about 1,000 predefined trees. A significantly lower number of predefined trees renders the method more sensitive. The final prediction is the sum of all trees such that the closest fit of input data and algorithm output is achieved. A mean-squared-error (MSE) loss function is minimized using gradient descent.

Gradient boosting algorithm, as implemented in the XGB library version 0.9 with the scikit-learn wrapper (Chen & Guestrin, 2016), is used to find a non-linear relationship between a suite of input features and the misfit

Table 2
Summary of the Products, Variables, and Data Processing Steps Used for Feature and Target Variables

Group: product	Variable	Abbreviation	Processing
SOCATv2019 ^a	Partial pressure of ocean CO ₂	pCO ₂	See Section 2.1
NOAA:OISSTv2 ^b	Sea Surface Temperature	SST	-
	SST seasonal anomaly	SST'	SST - annual average
	Sea Ice Fraction	ICE	-
Met Office:EN4 ^c	Sea Surface Salinity	SSS	-
NOAA:GLOBALVIEW ^d	Atmospheric CO ₂ mixing ratio	xCO ₂	-
DeBoyer:Mixed Layer Depth ^e	Mixed Layer Depth	MLD	log ₁₀ (MLD)
ESA:GlobColour ^f	Chlorophyll-a	Chl a	log ₁₀ (Chl a)
	Chl a seasonal anomaly	Chl a'	chl a - annual average
-	Day of year	J ₁	sin($\frac{j*2\pi}{365}$)
		J ₂	cos($\frac{j*2\pi}{365}$)
-	n-vector	A	sin(λ)
		B	sin(μ) cos(λ)
		C	- cos(μ) cos(λ)

Note. Data processing is described in the text. Symbol next to each product identifies the source.

^aReference: Bakker et al. (2016) Source: <https://www.socat.info/>. ^bReference: Reynolds et al. (2002) Source: <https://www.esrl.noaa.gov/psd/data/gridded/data.noaa.oisst.v2.html>. ^cReference: Good et al. (2013) Source: <https://www.metoffice.gov.uk/hadobs/en4/>. ^dReference: Conway et al. (1994) Source: <https://gml.noaa.gov/ccgg/mbll/>. ^eReference: de Boyer Montégut et al. (2004) Source: <http://www.ifremer.fr/cerweb/deboyer/mld/home.php>. ^f Reference: Maritorea et al. (2010) Source: <http://www.globcolour.info/>.

between each GOBM and SOCAT pCO₂: (pCO_{2,SOCAT} - pCO_{2,GOBM}). This algorithm was chosen because it leads to a better fit to input data than the other options considered, neural network or random forest (Stamell et al., 2020). To estimate pCO₂ at each spatial location, the algorithm relies on datasets with full, or approximately full, global coverage (Table 2): SST and Surface Chlorophyll-a (Chl-a) from satellite; Sea Surface Salinity (SSS) from a compilation of in-situ data sources (See Good et al., 2013 for a discussion of the data sources); Mixed layer depth (MLD) climatology from Argo floats; and atmospheric CO₂ mixing ratio (xCO₂) from station sites. These variables serve as proxies for known processes affecting pCO₂. Solubility is set by SSS and SST. Biological uptake of dissolved inorganic carbon (DIC) is indicated by Chl-a. Biological productivity and entrainment of DIC are influenced by MLDs. The long-term growth of ocean pCO₂ is driven by atmospheric xCO₂. Additional annual mean anomaly features are derived for SST and Chl-a by subtracting the annual mean from each year. These features help the algorithm learn more complex relationships and capture intra-annual variability. N-vector transformation (Gade, 2010; Gregor et al., 2017; Sasse et al., 2013) of latitude and longitude is included to help the algorithm learn spatial relationships. Although latitude and longitude do not have a direct mechanistic link to pCO₂, they are found to improve the reconstruction. This is attributable to these variables being proxies for biogeographic properties that structure pCO₂ fields (Fay & McKinley, 2013, 2017). Time transformation of the day of year constrains seasonality.

The features and associated pCO₂ misfit are split into three sets: validation, training, and testing. The test set is chosen as seven randomly selected years (1984, 1987, 1992, 1999, 2002, 2005, and 2014), these years account for about 16% of the data; thus we reserve approximately 20% of data for testing, as is standard in machine learning applications. The withheld test set is used to evaluate performance on a completely independent data set, individual years are withheld for the test set to retain individual ship tracks and increase the independence of test data from training and validation data (Gregor et al., 2019). The remaining data is randomly split between the validation and training set. The validation set, which accounts for 20% of the remaining data, is used to optimize the algorithms hyperparameters. The hyperparameters define the architecture of decision trees used in the model. The remaining data defines the training set, which is used to construct the decision trees (Gregor et al., 2019).

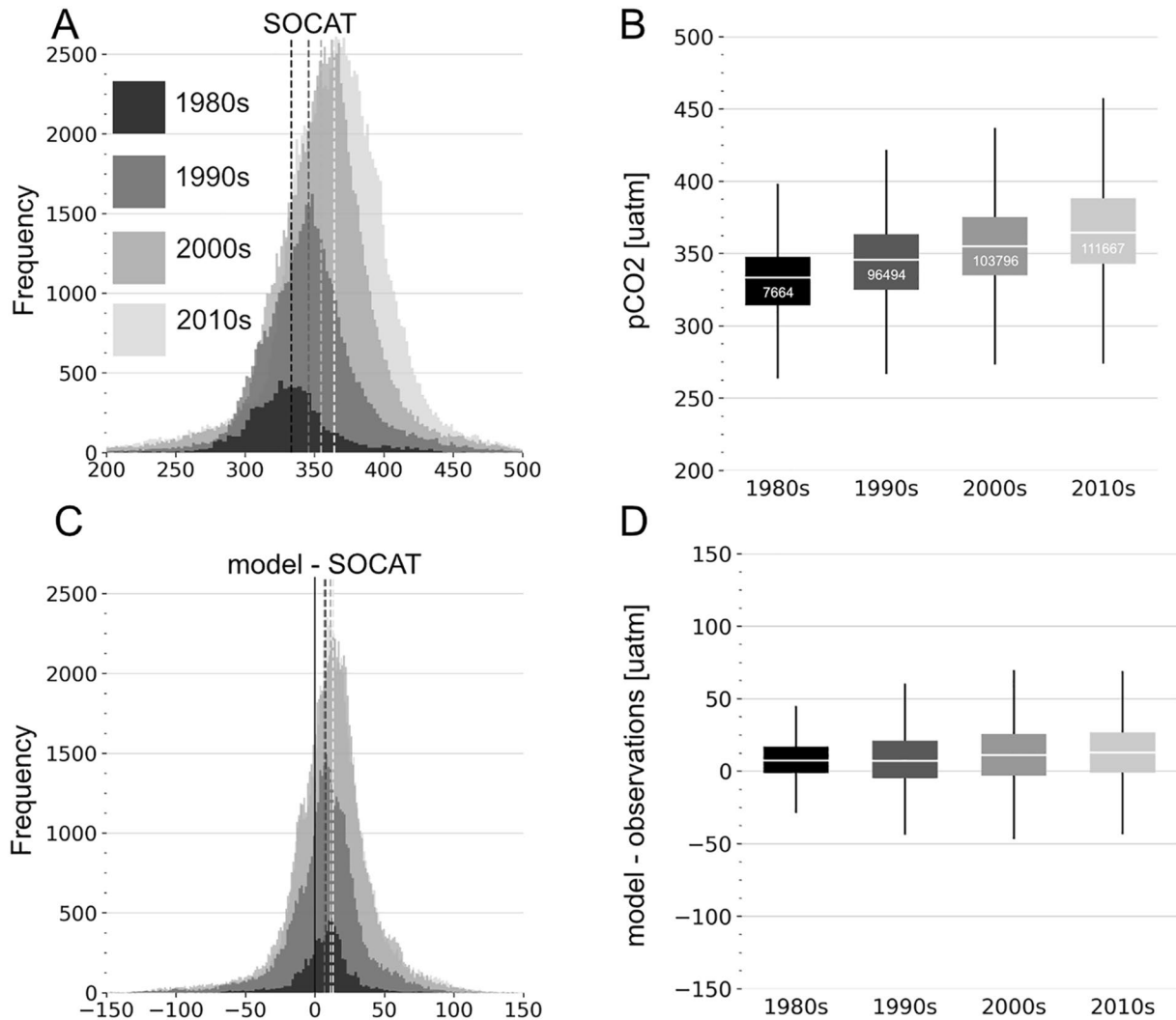


Figure 2. (a) Histogram of Surface Ocean CO₂ Atlas (SOCAT) pCO₂ observations in 1980s, 1990s, 2000s and 2010s shown by different shades of gray. Dotted line indicates mean pCO₂. (b) Boxplot of observations for each decade. Whisker indicates 1.5*IQR, observations outside the whisker have been omitted. White line indicates the mean and the number inside in the box indicates the number of observations within that decade. (c) Histogram of the difference between CESM model and SOCAT and (d) is the corresponding boxplot. Due to different internal model structures, the long-term trend from 1980s to 2010s varies from $-7 \mu\text{atm}$ to $+9 \mu\text{atm}$.

Our XGB algorithm uses 1,500 decision trees each with a max depth of nine levels or until no further splits to the samples in that node are possible. Each new tree uses 95% of the features and a random subsample of 85% of the observations from the training set with replacement. The weight of each sequential tree is reduced by 5%. Light L1 regularization was applied to control overfitting and loss is measured using MSE.

XGB is used to estimate spatio-temporal estimates of the misfit for each of nine GOBMs. Misfit estimates at all locations in space and time are added back to the original GOBM to correct the GOBM toward the data. This process is repeated for each of the nine GOBMs. The final result is then the average of all nine predictions. A schematic of HPD is shown in Figure 3.

2.4. Independent Data Sets

Observations not included in the SOCAT database are used to validate the method (Table 3). These datasets include the Lamont-Doherty Earth Observatory (LDEO) database, with SOCAT data removed; and GLObal Ocean Data Analysis Project version 2 (GLODAPv2). Two time series sites are also used for validation: Bermuda Atlantic Time-series Study (BATS) and Hawaii Ocean Time-series (HOT). In these datasets, pCO₂ is either

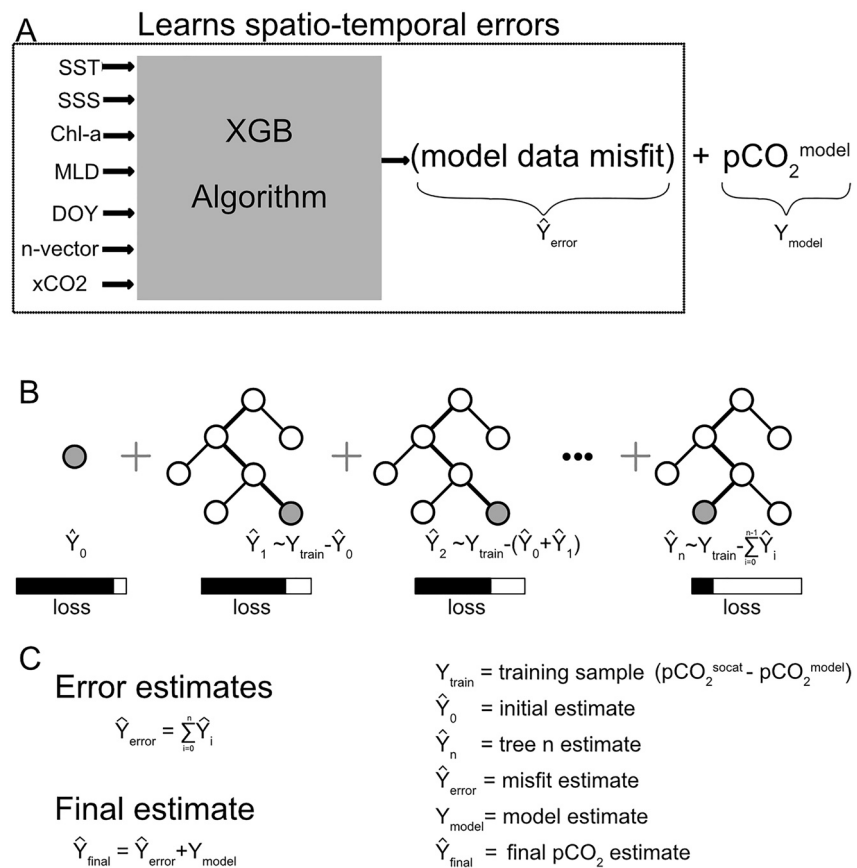


Figure 3. (a) Schematic of Lamont Doherty Earth Observatory-Hybrid Physics Data method. A relationship between a suite of auxiliary features and the model data misfit is learned via the eXtreme Gradient Boosting (XGB) algorithm. Spatio-temporal errors are then added back to the model's $p\text{CO}_2$ field to create the final product. (b) Outlines the XGB algorithm, where decision trees are sequentially added to improve the mistakes of the previous trees. Each additional tree reduces the loss and improves the overall performance of the algorithm. (c) The final estimate of $p\text{CO}_2$ is the model-data misfit estimated at all global points plus the original model. This process is done independently for each of the nine global ocean biogeochemical models and the final estimate is the average $p\text{CO}_2$.

directly measured or inferred from observations using carbonate system calculations with inputs of DIC and Total Alkalinity (TA). No data from GLODAPv2, BATS, or HOT are in the SOCAT database since $p\text{CO}_2$ is not directly measured at these sites, but instead is derived from DIC and TA. The cbsyst package (Hain et al., 2015) is used for carbonate system calculations. For decadal comparisons, timeframes are 1990s (1990–1999), 2000s (2000–2009) and 2010s (2010–2018).

The uncertainty in derived $p\text{CO}_2$ is dependent on the accuracy of the input measurements. For the modern ocean, cbsyst calculations are consistent with the constants of Lueker et al. (2000), and result in a 1.9% standard deviation in $p\text{CO}_2$ when DIC and TA uncertainties are 2.0 and 4.0 mol kg^{-1} , respectively. However, $p\text{CO}_2$ at

Table 3
Validation Datasets, Accuracy of $p\text{CO}_2$, and Total Number of $1^\circ \times 1^\circ$ Grid Points Is Shown for Each Data Set

Data set	Accuracy (μatm)	Grid points	Reference
LDEO database version 2018 ^a	$\pm 2.5 \mu\text{atm}$	16,161	Takahashi et al. (2019)
GLODAPv2 ^b	$>12 \mu\text{atm}$ at $400 \mu\text{atm}$	5,976	Olsen et al. (2019)
BATS ^b	$4 \mu\text{atm}$ at $400 \mu\text{atm}$	246	Bates (2007)
HOT ^b	$<7.6 \mu\text{atm}$ at $400 \mu\text{atm}$	214	Dore et al. (2009)

^a $p\text{CO}_2$ measured with $p\text{CO}_2$ equilibrator. ^b $p\text{CO}_2$ estimated from DIC and TA.

temperatures below 8°C may be underestimated using the Lueker et al. (2000) constants (Sulpis et al., 2020). For GLODAP, Bockmon and Dickson (2015) suggests an uncertainty of $5 \frac{\mu\text{mol}}{\text{kg}}$ for DIC and TA, thus suggesting an uncertainty greater than 1.9%. Gregor et al. (2019) estimate the uncertainty of GLODAP pCO₂ to be >12 μatm at 400 μatm. Although the measurements have high uncertainty, given the sparsity of the SOCAT database, including GLODAP as a validation data set outweighs its omission, consistent with previous studies (Gregor et al., 2019; Gregor & Gruber, 2021). At BATS the uncertainty is about 4 μatm (Bates, 2007) while at HOT it is <7.6 μatm (Dore et al., 2009). LDEO pCO₂ has uncertainty of 2.5 μatm (Takahashi et al., 2019).

2.5. Regression Metrics

A suite of regression metrics are used to compare the predictions (P) to the observations (O ; Stow et al., 2009). Metrics considered include correlation (r), bias, and root mean squared error (RMSE). Multiple metrics are considered in order to provide a thorough appraisal of each method. Metrics are displayed in a Taylor diagram (Taylor, 2001).

Pearson correlation coefficient (r) measures the tendency of the predicted and observations to vary together, bounded between, $-1 < r < 1$, with values near 1 indicating that they vary together and -1 indicating an inverse relationship. Correlation is also a measure of how well the phase is captured. Values near 1 and -1 indicate that the predictions and observations are perfectly in or out of phase, respectively. Intermediate values indicate a phase shift between the two signals, with values closer to zero indicating a larger phase shift between signals. The squared correlation r^2 , or coefficient of determination, represents the variance explained by the regression. Correlation is defined as the covariance between predictions and observations divided by the product of their standard deviations, $r = \frac{\text{cov}(P,O)}{\sigma_P \sigma_O}$, σ_P and σ_O represent the standard deviation of the predictions and observations, respectively.

Bias, average absolute error (AAE), and RMSE each measure the size of discrepancies, with values near zero indicating a close match between predictions and observations. However, each metric has strengths and weaknesses. Bias is simply calculated as the long-term mean difference between predictions and observations ($\text{bias} = \overline{P} - \overline{O}$), where overbars represent the temporal mean. Positive and negative bias values indicate predictions that are generally overestimated and underestimated respectively. Thus, bias provides a measure of the direction of discrepancy. However, bias values falling close to zero can be misleading with significant positive offsets at one point in space or time canceling out significant negative offsets elsewhere. $\text{RMSE} = \sqrt{\overline{(P - O)^2}}$ measures of the magnitude of discrepancy, but squaring the misfit makes RMSE sensitive to outliers. Alternatively, $\text{AAE} = \overline{|P - O|}$ treats each misfit equally, but is a less commonly used metric. We report bias, AAE and RMSE since each one provides a different insight into the goodness-of-fit.

2.6. Area Coverage

The LDEO-HPD product covers 89.6% of the total ocean area, leaving out the Arctic and coastal zones. Before estimating the net carbon flux from observation-based products, we use the method of Fay et al. (2021) to fill spatial gaps in the pCO₂ product with climatology (Landschützer, Laruelle, et al., 2020) plus the global-mean trend. This fills in the 10.4% to create a global gap-free product. Climatological filling lowers global mean pCO₂ from 356 to 352 μatm in the final product. This climatological filling technique (Fay et al., 2021) was also applied to each observational data product to which we compare our results (Table 5).

2.7. Air-Sea CO₂ Flux

The air-sea CO₂ exchange was calculated using a bulk parameterization (Equation 2):

$$F_{CO_2} = k_w S_{CO_2} (1 - f_{ice}) (pCO_2^{\text{atm-moist}} - pCO_2^{\text{ocean}}) \quad (2)$$

which parameterizes the air-sea CO₂ flux (F_{CO_2}) as a function of the gas transfer velocity (k_w), CO₂ solubility (S_{CO_2}), ice fraction (f_{ice}), and partial pressure of CO₂ in moist air ($pCO_2^{\text{atm-moist}}$) and surface ocean (pCO_2^{ocean}).

Table 4
Wind Speed Products Used to Calculate CO₂ Flux

Wind speed product	Reference
CCMPv2.0 ^a	Mears et al. (2019)
ERA5 ^b	Hersbach et al. (2020)
JRA-55 ^c	Harada et al. (2016)

^aSource: <http://www.remss.com/measurements/ccmp/>. ^bSource: <https://www.ecmwf.int/en/forecasts/datasets/reanalysis-datasets/era5>. ^cSource: <https://jra.kishou.go.jp/JRA-55/>.

Solubility is calculated following Weiss (1974) and partial pressure of moist air ($pCO_2^{atm-moist}$) is calculated following Equation 3,

$$pCO_2^{atm-moist} = xCO_2(P_{atm} - p_{H_2O}) \quad (3)$$

where xCO_2 is the dry air mixing ratio of atmospheric CO₂, P_{atm} is the total atmospheric pressure, and p_{H_2O} is the saturation vapor pressure (Dickson et al., 2007). We use the Wanninkhof (1992) formulation for the gas transfer velocity (Equation 4):

$$k_w = k_{w,scalded} u^2 \left(\frac{Sc}{660} \right)^{-0.5} \quad (4)$$

which parameterizes k_w as a function of wind speed squared (u^2) and the Schmidt number (Sc). k_w is scaled by a factor of $k_{w,scalded}$ for each wind product to match the invasion of bomb ¹⁴C ($343 \pm 40 \times 10^{26}$ atoms ¹⁴C as of 1994, see Sweeney et al., 2007) (Fay et al., 2021). Three wind products were used (Table 4). Flux was calculated separately for each wind product and then averaged to create the final best estimate.

pCO₂ measured in situ and compiled in the SOCAT database is set by the combination of the anthropogenic and natural background carbon cycles. Thus, the calculated flux is the net, or contemporary, flux (F_{NET}).

2.8. Estimating Anthropogenic Carbon Flux From the Net Flux

The net CO₂ flux is the sum of an anthropogenic and a natural component ($F_{NET} = F_{NAT} + F_{ANT}$). Surface ocean pCO₂ quantifies F_{NET} , while interior ocean data quantify F_{ANT} . Closure terms are required to compare these independent quantifications of the ocean carbon sink.

The dominant net air-sea flux due to the natural carbon cycle is the slow outgassing of riverine carbon by the ocean (Aumont et al., 2001). The community's estimate of the net riverine-induced carbon outgassing (F_{RIV}) is still evolving. Here we use an average of three estimates representing the spread of the available approaches: a geochemical budgeting perspective ($+0.45 \pm 0.18$ PgC/yr; Jacobson et al., 2007), a meridional heat constraint approach ($+0.78 \pm 0.41$ PgC/yr; Resplandy et al., 2018), and a process-based ocean model ($+0.23$ PgC/yr; Lacroix et al., 2020). Since no uncertainty is presented for the Lacroix et al. (2020) estimate, we assume a 50% 1σ uncertainty, which is consistent with the relative magnitude of uncertainty for the other two estimates. Combining these three estimates, we derive an estimate of carbon efflux due to river inputs to the ocean in the observation-based product flux estimates of $+0.49 \pm 0.26$ PgC/yr. This $F_{RIV} \approx F_{NAT}$ will be removed from F_{NET} estimates from HPD and other products to arrive at F_{ANT} .

Anthropogenic carbon accumulation can be estimated from interior ocean observations, for which a global survey is completed approximately once per decade, and thus this component is estimated over a defined time period. Gruber, Clement, et al. (2019) find F_{ANT} at -2.6 ± 0.3 PgC/yr for 1994–2007. A changing ocean circulation may have modified F_{NAT} over 1994–2007 through a non-steady state outgassing flux of natural carbon. Thus, a natural non-steady state flux ($F_{NAT,NS}$) has been proposed (Gruber, Clement, et al., 2019), that is, $F_{NAT} = F_{NAT,NS} + F_{RIV}$. Applying the transient steady state assumption to F_{NET} from one observation-based product (Landschützer et al., 2016), Gruber, Clement, et al. (2019) find $F_{NAT,NS} = +0.38$ PgC/yr. However, the transient steady state assumption is known to hold when atmospheric carbon accumulation is exponential, and this has not been the case in recent decades (Raupach et al., 2014; Ridge & McKinley, 2020). This estimate of $F_{NAT,NS}$ is likely an upper bound. Nevertheless, we follow Gruber, Clement, et al. (2019) and adjust their F_{ANT} estimate by this amount.

Adjusting the F_{ANT} estimate of Gruber, Clement, et al. (2019) leads to $F_{ANT} + F_{NAT,NS} = -2.2 \pm 0.3$ PgC/yr for 1994–2007. Earlier, for the IPCC AR4, Denman et al. (2007) synthesized multiple estimates from ocean and atmosphere tracer studies to estimate $F_{ANT} = -2.2 \pm 0.4$ PgC/yr for 1990–1999, and without any adjustment for $F_{NAT,NS}$. We compare estimates of $F_{NET} - F_{RIV}$ from LDEO-HPD and other observation-based products (see Section 2.9) to these estimates.

Table 5
Observational Data Products for Comparison to These Results

Observation-based pCO ₂ product	Reference
MPI-SOMFFN	Landschützer et al. (2014); Landschützer, Gruber, et al. (2020)
JENA-MLS	Rödenbeck et al. (2014)
CMEMS	Denvil-Sommer et al. (2019)
CSIR	Gregor et al. (2019)

2.9. Observational-Based Products

We compare the pCO₂ error statistics and CO₂ flux estimates to four products that extrapolate from SOCAT data to global coverage using machine learning or other statistical modeling techniques (Table 5).

3. Results

With LDEO-HPD, an XGB algorithm estimates time-varying maps of model-data misfit, and these misfits are then used to adjust model fields to arrive at an estimate of the real-world pCO₂, from which CO₂ flux is then calculated. By identifying large-scale patterns of model mismatch with observations (Section 3.1), LDEO-HPD approach reconstructs real-world pCO₂ with greater fidelity than other recently published approaches (Section 3.2). After correcting for riverine outgassing, air-sea CO₂ flux estimates from LDEO-HPD are consistent with independent observations for both 1990–1999 and 1994–2007 (Section 3.3).

3.1. Model-Data Misfit

The 9-model, global-mean bias of 10 μatm in ocean pCO₂ (Figure 1d) can partially be attributed to neglecting to account for the water vapor correction when calculating the atmospheric pCO₂ that forces the model (Dickson et al., 2007). If the molar concentration of CO₂ is measured in dry air then, by standard protocol (Orr et al., 2017), the atmospheric partial pressure of CO₂ must be reduced by the vapor pressure of water (Equation 3). This is typically a small percentage correction, but still a change in the pressure field of only 3% changes the partial pressure of CO₂ by about 10 μatm. Thus, if the water vapor correction is ignored, the partial pressure of CO₂ in the atmosphere that the ocean model experiences will be too high and ocean pCO₂ will also be high. Of the nine models, three do not account for this correction, and the other six do (Friedlingstein et al., 2020). Hauck et al. (2020) illustrate through comparison to SOCAT data that these models have a significant high bias in pCO₂. In addition, they show that several models that do include the water vapor correction also have a high pCO₂ bias, but do not identify the source of this error. The mean pCO₂ bias of +10 μatm that we find (Figure 1d) is thus partially, but not fully, attributable to several models not applying the water vapor correction.

The model corrections solved for by the XGB algorithm has significant spatial structure, and thus is doing far more than just addressing a global-mean bias in the GOBM priors. This is illustrated for two of the nine models in Figure 4. There are distinct patterns and consistent seasonality in the required corrections. For the MPI model, in the Southern Ocean and North Pacific, pCO₂ is far too high in winter (JJA) and far too low in summer (DJF), thus the XGB algorithm imposes strong negative and positive corrections, respectively. In the North Atlantic, however, winter is too low and summer is too high, requiring the opposite sign of corrections. In the subtropics, MPI requires a strong negative correction. For CNRM, these patterns are different, with the whole of the winter hemisphere generally being slightly too low in pCO₂ and the majority of the summer hemisphere being too high in pCO₂, requiring modest positive and negative correction, respectively. Both models require a positive correction in the equatorial Pacific. Zonal-average misfits (Figure 4b) indicate that both of these models require the same sign and comparable magnitude seasonal correction in the extratropical Northern Hemisphere, while MPI requires much larger corrections in the Southern Ocean.

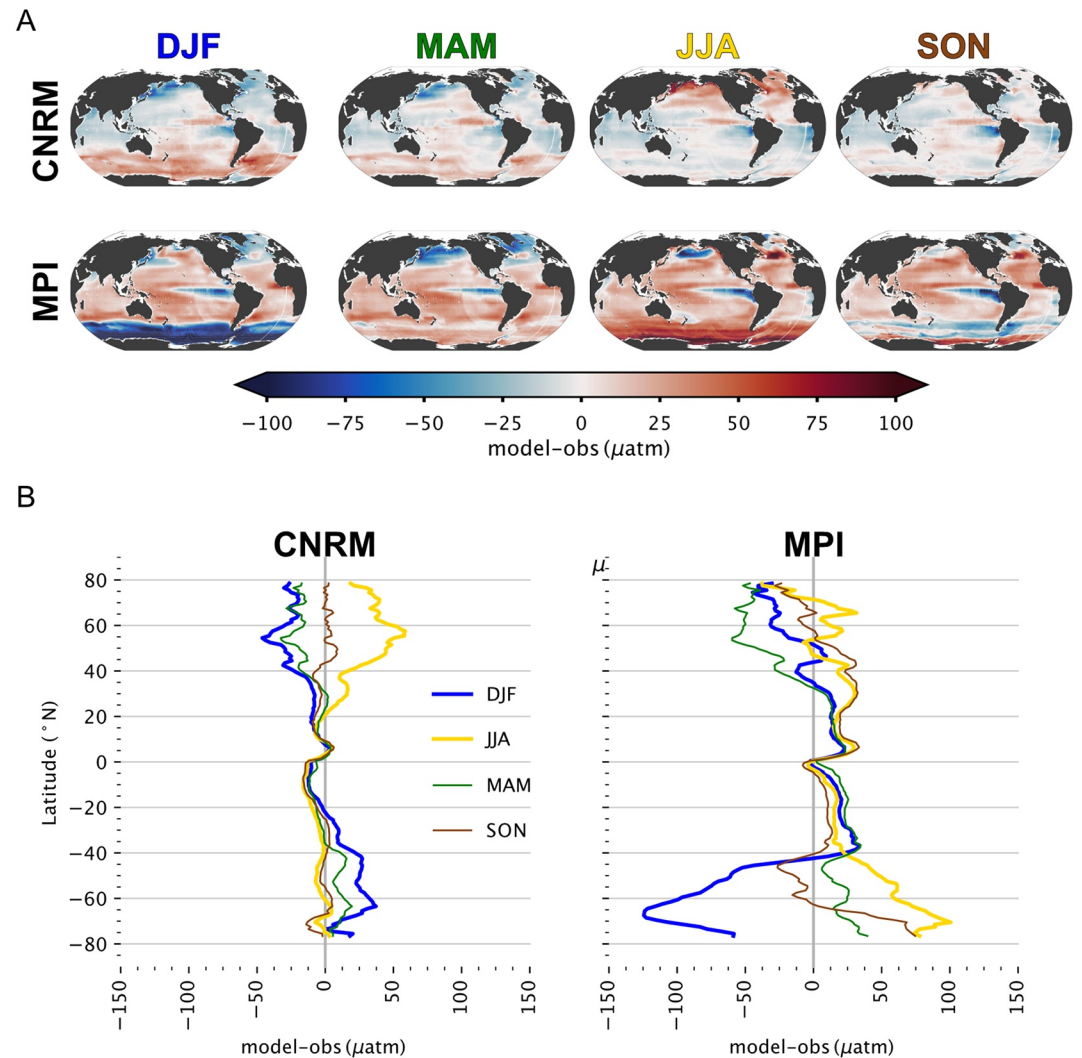


Figure 4. (a) Average pCO_2 misfit in the MPI and CNRM model for all years, December, January, and February (DJF); March, April and May (MAM); June, July, and August (JJA); and September October and November (SON). (b) Zonally average pCO_2 misfit in the MPI and CNRM models for DJF, JJA, MAM, and SON.

3.2. Evaluation of LDEO-HPD Against Independent Datasets

At the ocean timeseries sites at Bermuda (BATS) and Hawaii (HOT), LDEO-HPD compares quite favorably to the observations. The amplitude of seasonal and interannual variability in LDEO-HPD is as observed at HOT (Figures 5b and 6a) and slightly underestimated at BATS (Figures 5c and 6b), and the trends at both timeseries are well-represented. Compared to existing pCO_2 gap-filling methods, LDEO-HPD performs slightly better at BATS and HOT, with the lowest unbiased-RMSE relative to SOMFFN, MLS, and CMEMS (Figures 6a and 6b). Correlations are high at HOT and BATS because of the pronounced subtropical seasonality captured in the datasets. All these products are reliably able to capture subtropical seasonality (Gloege et al., 2021; Rödenbeck et al., 2015; Stamell et al., 2020).

LDEO and GLODAP are global observation datasets from intermittent ship transects. In these data, seasonality is less well-resolved, a fact that helps to explain the lower correlations of all products to the data relative to BATS and HOT. All the products show similar performance on LDEO observations, with all the products underestimating the variability (Figure 6c). For comparison to GLODAP, LDEO-HPD has a smaller unbiased-RMSE relative to other products (Figure 6d). LDEO-HPD and MLS capture the amplitude of variability in GLODAP equally well, and slightly better than SOMFFN and CMEMS.

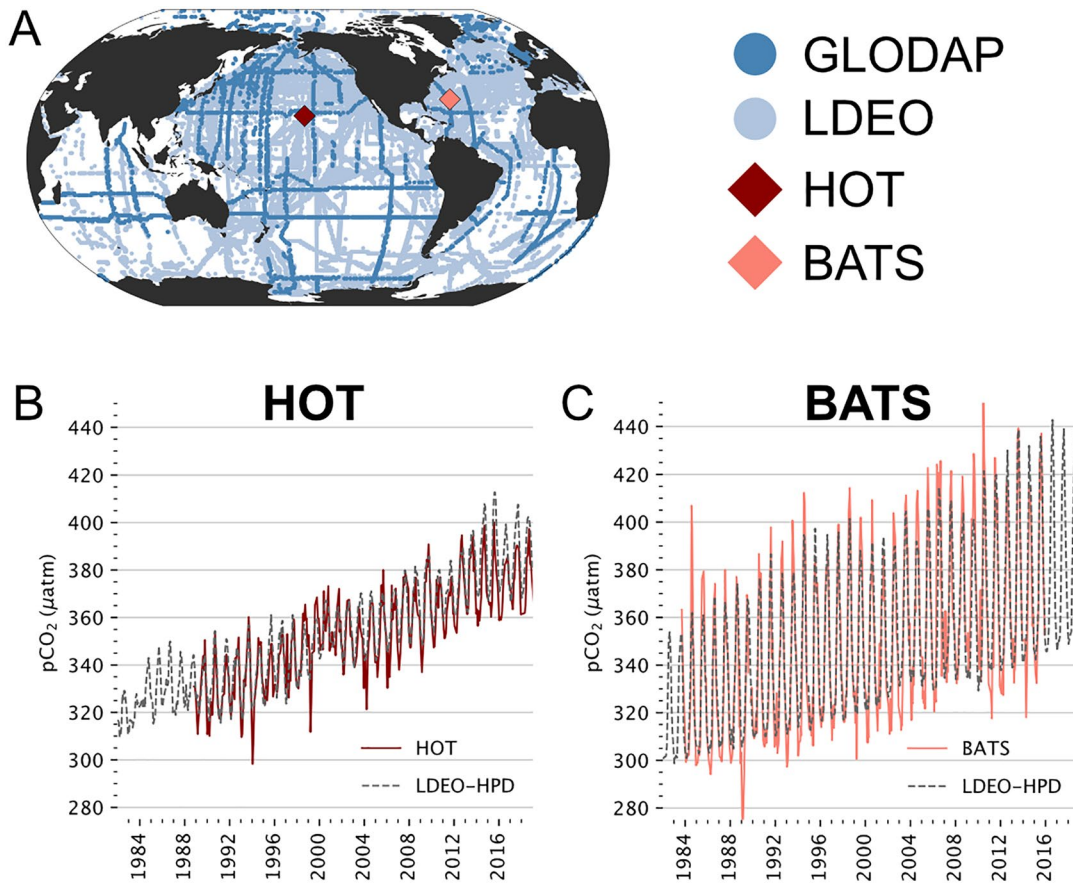


Figure 5. (a) Locations of independent datasets. Bermuda Atlantic Time-series Study (BATS) and Hawaii Ocean Time-series (HOT) are timeseries, while the GLODAP and Lamont-Doherty Earth Observatory are spatially varying. (b) Comparison of HOT with Lamont Doherty Earth Observatory-Hybrid Physics Data (LDEO-HPD) output. (c) comparison between BATS and LDEO-HPD output.

Over time, the skill of LDEO-HPD against independent observations of LDEO and GLODAP increases relative to the other methods. In the 1990s, the skill of all methods are indistinguishable (Figure 7, left). In the 2000s, comparison to GLODAP indicates that LDEO-HPD is slightly better than the others, though there is no distinction across the methods for LDEO (Figure 7, center). In the 2010s, LDEO-HPD clearly does the best job at capturing GLODAP, and is slightly improved against LDEO (Figure 7, right). Thus, we attribute the improved overall fit to independent observations (Figure 6) to the better fit in the later decades (Figure 7).

3.3. CO₂ Fluxes: 1982–2018

Mean pCO₂ and CO₂ flux from LDEO-HPD algorithm for 1982–2018 show well known features. Elevated pCO₂ is observed at the equator (Figure 8a), especially in the east-equatorial Pacific. This elevated pCO₂ is the result of upwelling of cold, carbon laden waters. The surface pCO₂ in this region is greater than the atmosphere, resulting in net CO₂ flux from the ocean to the atmosphere (Figure 8b).

Over time, the net global CO₂ flux has become increasingly negative (Table 6), that is, the ocean has become a greater net carbon sink over the recent decades as atmospheric pCO₂ has risen. Coastal filling (Section 2.6) increases uptake by nearly 0.1–0.2 PgC/yr, consistent with past estimates of globally integrated coastal uptake (Roobaert et al., 2019).

Applying the same to the calculation of air-sea CO₂ fluxes for all products (Section 2.7), and applying the F_{RIV} correction, we find that fluxes estimated by LDEO-HPD are within the range of the other products for F_{ant} (Figure 9a). Independent flux estimates based on interior data or atmospheric constraints also indicate consist-

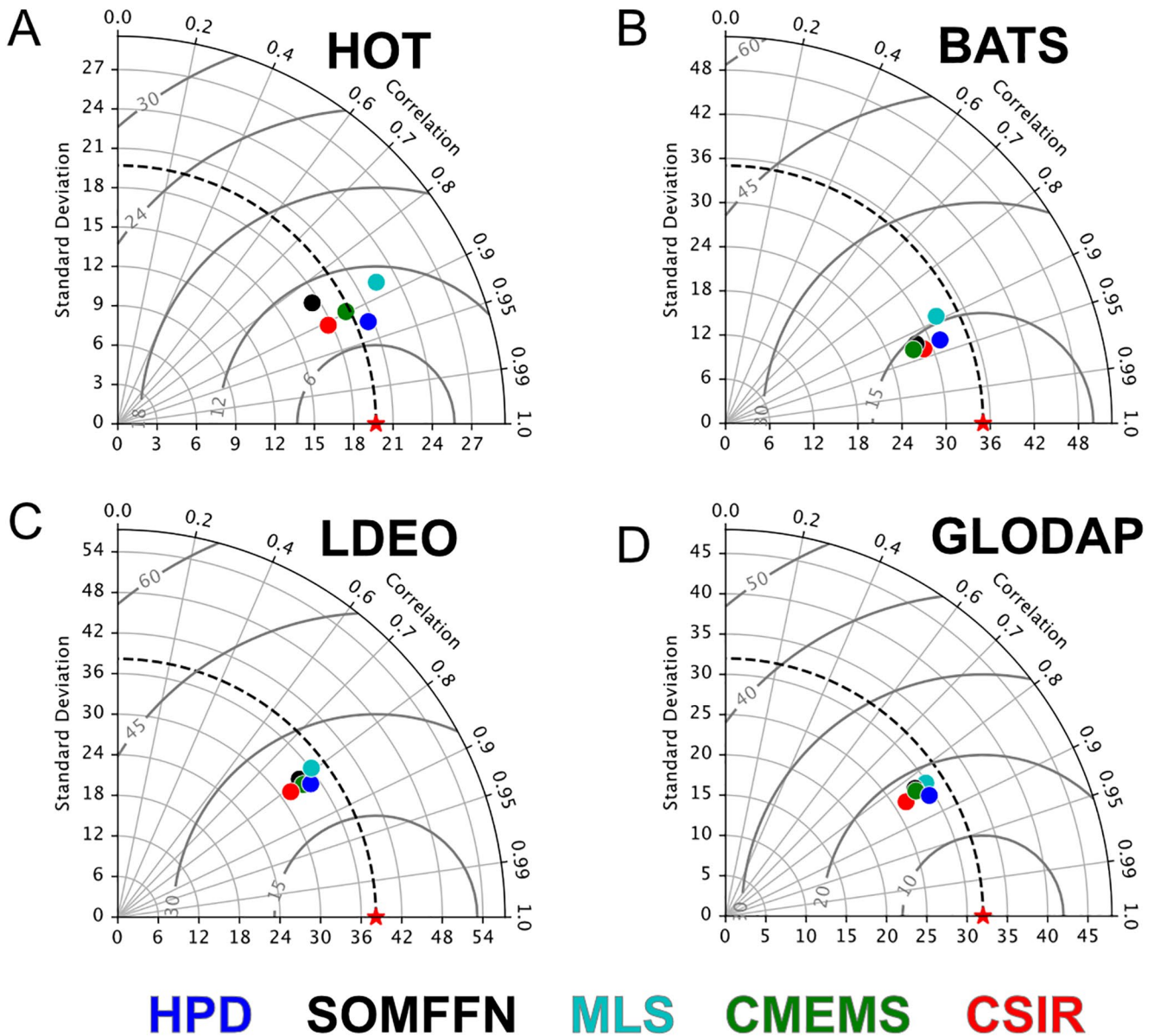


Figure 6. Taylor diagrams display the performance of published gap-filling techniques and Lamont Doherty Earth Observatory-Hybrid Physics Data (LDEO-HPD) product. Performance is evaluated at two timeseries: (a) Hawaii Ocean Time-series (HOT) and (b) Bermuda Atlantic Time-series Study (BATS); and two global datasets: (c) Lamont Doherty Earth Observatory and (d) GLODAP. Red star indicates standard deviation of each data set.

ency. Compared to F_{ANT} for 1990–1999 (Denman et al., 2007) and $F_{ANT} + F_{NAT,NS}$ 1994–2007 (Gruber, Clement, et al., 2019), all products are within the uncertainty bounds (Figure 9b).

Improved comparison to independent data in LDEO-HPD is consistent with the reduced skewness of the target variable distribution (Figure 2). Reduced skewness should particularly improve predictions at the tails of the distribution, which in this case are the decades of the 1980s and 2010s. We do not have sufficient independent data to make comparisons in the 1980s, but HPD performs best of all methods in the 2010s (Figure 7, Table 7).

4. Discussion

We show that incorporating physical models into machine learning algorithms results in some improvement in predictions of surface ocean pCO_2 . Using output from GOBMs as a prior guess allows us to reduce the skewness of the target variable distribution (Figure 2). Though GOBMs are imperfect representations of the real ocean (Hauck

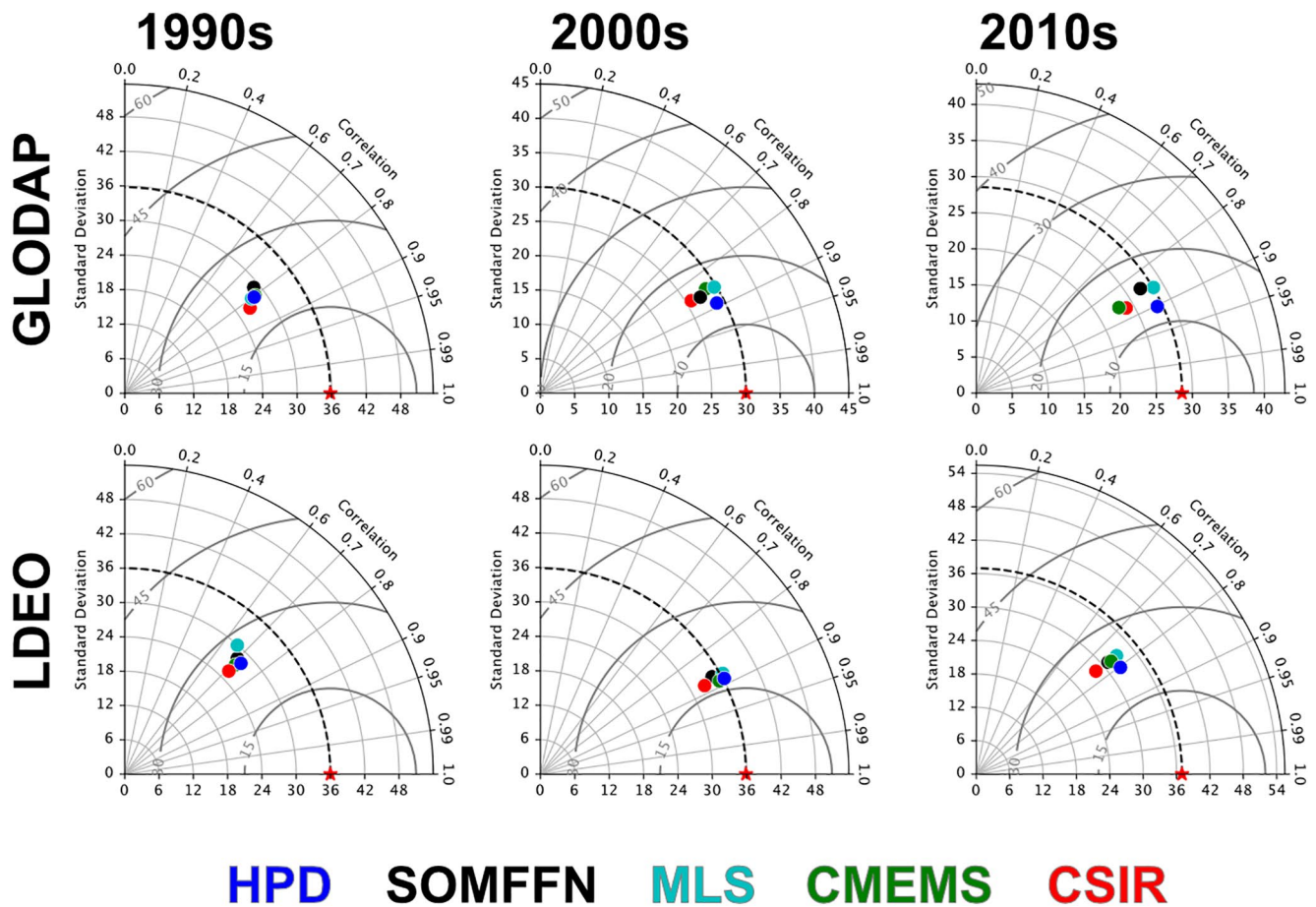


Figure 7. Taylor diagrams display the performance of published gap-filling techniques and Lamont Doherty Earth Observatory-Hybrid Physics Data (LDEO-HPD) product. Performance is evaluated at two global data sets, Lamont Doherty Earth Observatory and GLODAP, using data from 1990 to 1999 (1990s), 2000–2009 (2000s), and 2010–2018 (2010s). Red star indicates standard deviation of each data set.

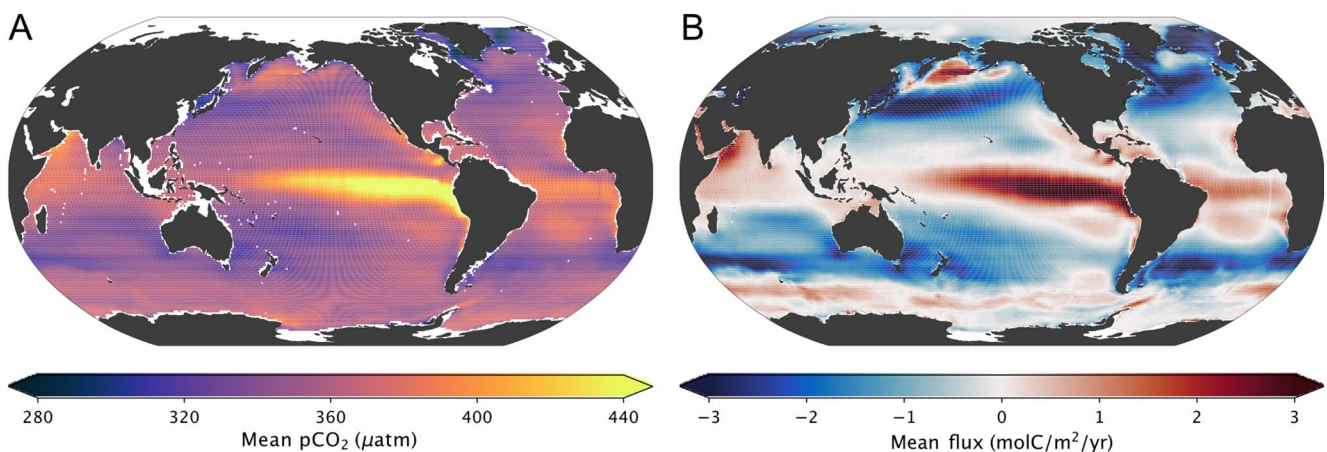


Figure 8. Mean (a) $p\text{CO}_2$ and (b) net CO_2 flux over 1982–2018 estimated from Lamont Doherty Earth Observatory-Hybrid Physics Data (LDEO-HPD). A spatially complete map of CO_2 flux is achieved by filling in gaps with a trend plus climatology.

Table 6
Net CO₂ Flux (F_{NET}) (PgC/yr) From LDEO-HPD Across Decades Without Coastal Filling (“Unfilled”) and Filled With the Climatology (Section 2.6)

	Unfilled	Filled
1982–1990	−1.38	−1.53
1990–2000	−1.48	−1.65
2000–2010	−1.49	−1.69
2010–2018	−1.96	−2.23

et al., 2020), this work illustrates that they can provide useful prior estimates of pCO₂ upon which data can improve using machine learning algorithms. By merging models and data, LDEO-HPD reduces error in estimates of pCO₂ (Figure 6), with the recent decades being the most improved (Figure 7, Table 7).

The LDEO-HPD approach of correcting GOBMs estimates the misfit between model output and observed pCO₂ at all points in space and time (Figure 3). The seasonality of model-data misfits (Figure 4) indicate that the LDEO-HPD is correcting for errors in model representation of seasonal physical and biogeochemical processes, such as mixed layer deepening and biological processes. These machine-learning derived maps of model-data misfit could be applied as a diagnostic of model performance to offer a larger-scale perspective that

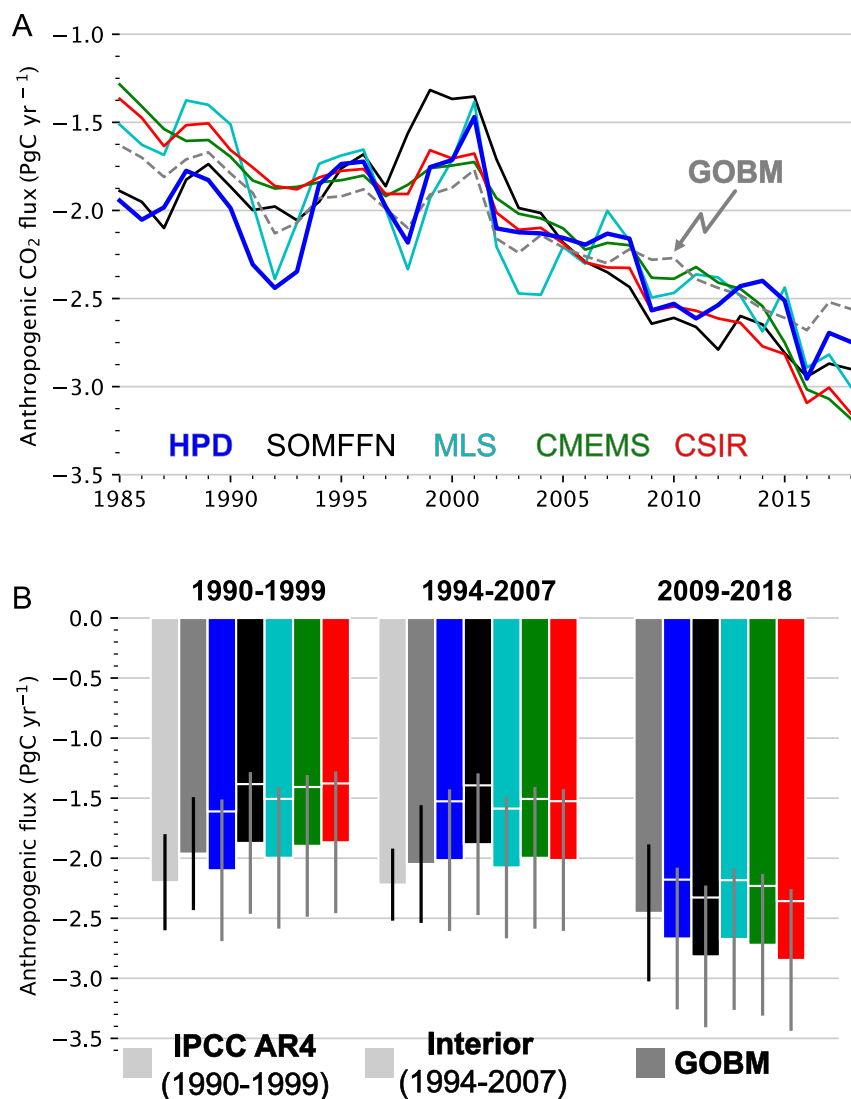


Figure 9. (a) Anthropogenic air-sea CO₂ exchange (F_{ANT}) for 1985–2018 from Lamont Doherty Earth Observatory-Hybrid Physics Data (LDEO-HPD) and four other products: SOMFFN, MLS, CMEMS, CSIR-ML6. Positive is to the atmosphere. Gray dash is the mean of the nine Global Ocean Biochemical Model (GOBM) priors, which are also the basis for the ocean sink estimate of the Global Carbon Budget 2020 (Friedlingstein et al., 2020). (b) Anthropogenic CO₂ flux for 1990–1999, 1994–2007, and 2009–2018. Light gray bar indicates IPCC AR4 or interior observation-based estimates with uncertainty. Dark gray bar is the mean of the nine GOBMs. Colored bars indicate observation-based estimates. The white line separates F_{NET} from the products and F_{RIV} , estimated as the average of three estimates (0.49 PgC/yr), see Section 2.8. Thin lines indicate uncertainty; product uncertainty is estimated to be 0.6 PgC/yr, see Section 4.

Table 7
RMSE at Independent Datasets Across Decades in Each Product Against GLODAP and LDEO Datasets Across Three Decades: 1990s, 2000s, and 2010s

	1990s	2000s	2010s
LDEO-HPD	22.0 (27.6)	<u>13.8</u> (19.0)	<u>15.4</u> (23.4)
SOMFFN	23.3 (28.2)	15.4 (19.9)	16.9 (26.0)
MLS	22.2 (32.7)	16.1 (25.5)	17.7 (31.6)
CMEMS	21.9 (25.8)	16.2 (18.6)	15.9 (24.8)
CSIR	<u>20.8</u> (28.4)	15.6 (21.2)	15.7 (27.9)

Note. Underlined values indicate the product with the lowest RMSE. LDEO values are shown in parenthesis.

complements direct comparison to in situ data (Hauck et al., 2020). Model development could be supported with this approach to model-data comparison.

LDEO-HPD indicates an ocean carbon sink that is on the upper end of the suite of products for 1990–1999, but at the lower end of the suite of products for 2009–2018 (Figure 9). This may be due to reduced skewness in the target variable in this approach. The observed pCO₂ distribution is centered somewhere between the 1990s and 2000s (Figures 2a and 2b). The pCO₂ observed in the 1980s and 1990s is lower than this long-term mean pCO₂ due to the long-term increase of surface ocean pCO₂ in response to atmospheric pCO₂ growth, similarly the pCO₂ of the 2000s and 2010s is higher. This has the potential to skew pCO₂ predictions from machine learning algorithms in the 1980s and 1990s slightly high, and in the 2000s and 2010s slightly low, in both cases toward the mean of the overall distribution. This effect could help to explain the positive pCO₂ bias between 1982 and 1993 in the reconstruction of Gregor et al. (2019). Since LDEO-HPD has a reduced skewness in its target variable

(Figures 2c and 2d), this potential issue should be minimized. Nevertheless, it is important to note that Landschützer et al. (2014) do not find a temporal trend in RMSE or bias for their product over 14 years (1998–2011). Yet, this is half the number of years as considered here, and any impact of skewness should increase with longer timeseries.

Machine learning algorithms are based on the assumption that training and testing data are independent and identically distributed and thus drawn from the same data generating distribution (Goodfellow et al., 2016). A tighter distribution, such as when the mean is not shifting over time, should be easier for a statistical algorithm to fit. By LDEO-HPD fitting model-data misfit, the skewness of the target variable distribution is largely eliminated (Figures 2c and 2d). This reduction of skewness in LDEO-HPD (Figures 2a and 2b) is consistent with both the improved fit to independent pCO₂ observations, particularly in later years (Figure 7, Table 7) and with the slightly larger ocean carbon sink LDEO-HPD in the 1990s and the slightly smaller sink since 2009 (Figure 9).

Here, we provide hints that temporal skewness of the pCO₂ training data may be impacting the current suite of observation-based products and LDEO-HPD's comparison to them. However, we do not prove this a significant issue. A comprehensive assessment is clearly needed, particularly in light of the strongly increasing product-based ocean carbon sink estimates since 2005 that increasingly diverge from models (Friedlingstein et al., 2020; Hauck et al., 2020). If the ocean sink is, in fact, growing much more rapidly than currently estimated by the Global Carbon Budget, this would imply much smaller trends must be occurring in carbon uptake by the land biosphere. A comprehensive study of this issue for the ocean products could be facilitated by tools such as the Large Ensemble Testbed (Gloege et al., 2021).

The combination of data-based machine learning with specific physical constraints or with the physics embodied in dynamical models is an emerging concept for earth science applications (Karpatne et al., 2017; Reichstein et al., 2019). As in other efforts that have corrected dynamical models using observations (Watt-Meyer et al., 2021), we use GOBMs as a prior estimate of the surface ocean pCO₂ field, and then correct these fields with data. The fact that the distribution of the target variable is substantially tightened (Figures 2a and 2c) suggests that GOBMs bring valuable prior physical information to support a robust reconstruction. For example, where pCO₂ is high, such as in the equatorial Pacific, it is also high in the model; and thus model-data misfits are constrained in magnitude (Figure 2c). If the GOBMs did not provide a useful prior, that is, had little relationship to the observations, the spread of model-data misfit would be expected to be larger than of pCO₂ alone. Tightening the distribution of the target variable supports our improved machine learning based predictions (Figures 6 and 7).

Gregor et al. (2019) suggest we may have “hit a wall” in our ability to extrapolate sparse pCO₂ data to global coverage. Here, we illustrate that incorporating model output and addressing skewness of the target variable distribution allows some additional improvement in prediction skill. In addition, LDEO-HPD employs an XGB algorithm, which is also found to be promising by Gregor et al. (2019). Stamell et al. (2020) showed the XGB algorithm performs slightly better in pCO₂ extrapolation than neural network or random forest algorithms. XGB's strength is its self-correcting nature in which each additional tree improves upon errors made in the previous.

For 2009–2018, the Global Carbon Budget 2020 (Friedlingstein et al., 2020) indicates an ocean anthropogenic sink (F_{ANT}) of -2.5 ± 0.6 PgC/yr (Figure 9). LDEO-HPD indicates a similar flux, -2.6 ± 0.6 PgC/yr ($F_{\text{ANT}} = F_{\text{NET}}$ —

F_{RIV}). The standard deviation across the nine error-corrected GOBMs (0.1 PgC/yr), the uncertainty associated with F_{RIV} (0.26 PgC/yr) and a 20% uncertainty from Wanninkhof (2014) associated with the gas transfer velocity (0.52 PgC/yr) are added in quadrature to produce the total uncertainty of LDEO-HPD. The other four products discussed here (Table 5) have mean uptake of -2.6 ± 0.6 to -2.8 ± 0.6 PgC/yr, using $F_{RIV} = +0.49 \pm 0.26$ PgC/yr to calculate F_{ANT} from F_{NET} for all and including a 20% uncertainty associated with the gas transfer velocity. Thus, all products are consistent with the Global Carbon Budget 2020.

It is important to note that our updated estimate of F_{RIV} is lower than that used by the Global Carbon Budget 2020 (+0.61 PgC/yr), and by Hauck et al. (2020) (+0.78 PgC/yr), thus reducing the apparent model to observation-based product discrepancy that has been previously discussed (Friedlingstein et al., 2020). In addition, the harmonized flux calculation approach used here slightly reduces ocean uptake for some products (Fay et al., 2021). In summary, for 2009–2018, we find that all products fall within the uncertainties of the Global Carbon Budget 2020 for F_{ANT} , with LDEO-HPD on the lower end of the range and slightly closer to the Global Carbon Budget 2020 mean.

5. Conclusions

To reconstruct the real ocean's surface ocean pCO_2 , LDEO-HPD rectifies output of nine GOBMs by learning the misfit from observed pCO_2 using an XGB algorithm and observed driver fields. LDEO-HPD improves prediction accuracy compared to other state-of-the-art pCO_2 data products, as indicated by improved fit to independent pCO_2 data. This suggests that GOBM output adds useful prior information to machine learning for this application. In addition, the globally and temporally complete misfits learned by the algorithm additionally have promise as a new diagnostic and visualization tool with which GOBM performance can be assessed.

Adding physical information, here by using GOBMs as a prior, and addressing temporal skewness in surface ocean pCO_2 distribution offer promising directions for continued improvement in the fidelity of machine-learning based reconstructions of the ocean carbon sink. The LDEO-HPD suggests a global ocean sink for anthropogenic carbon that is within the range of the suite of existing pCO_2 observation-based products, and that is in agreement with the Global Carbon Budget 2020 (Friedlingstein et al., 2020).

Data Availability Statement

Analysis scripts and LDEO-HPD code is available at <https://github.com/iglloege/LDEO-HPD> and LDEO-HPD output is available at <https://zenodo.org/record/4760205>.

References

- Adcroft, A., Anderson, W., Balaji, V., Blanton, C., Bushuk, M., Dufour, C. O., et al. (2019). The GFDL global ocean and sea ice model om4. 0: Model description and simulation features. *Journal of Advances in Modeling Earth Systems*, 11(10), 3167–3211. <https://doi.org/10.1029/2019ms001726>
- Aumont, O., Éthé, C., Tagliabue, A., Bopp, L., & Gehlen, M. (2015). PISCES-v2: An ocean biogeochemical model for carbon and ecosystem studies. *Geoscientific Model Development Discussions*, 8(2), 2465–2513. <https://doi.org/10.5194/gmd-8-2465-2015>
- Aumont, O., Orr, J. C., Monfray, P., Ludwig, W., Amiotte Suchet, P., & Probst, J. L. (2001). Riverine-driven interhemispheric transport of carbon. *Global Biogeochem*, 15, 393–405. <https://doi.org/10.1029/1999gb001238>
- Bakker, D. C. E., Pfeil, B., Landa, C. S., Metzl, N., O'Brien, K. M., Olsen, A., et al. (2016). A multi-decade record of high-quality fCO_2 data in version 3 of the surface ocean CO_2 atlas (socat). *Earth System Science Data*, 8(2), 383–413. <https://doi.org/10.5194/essd-8-383-2016>
- Bates, N. R. (2007). Interannual variability of the oceanic CO_2 sink in the subtropical gyre of the north atlantic ocean over the last 2 decades. *Journal of Geophysical Research*, 112(C9), C09013. <https://doi.org/10.1029/2006jc003759>
- Berthet, S., Séférian, R., Bricaud, C., Chevallier, M., Voldoire, A., & Éthé, C. (2019). Evaluation of an online grid-coarsening algorithm in a global eddy-admitting ocean biogeochemical model. *Journal of Advances in Modeling Earth Systems*, 11(6), 1759–1783. <https://doi.org/10.1029/2019ms001644>
- Bockmon, E. E., & Dickson, A. G. (2015). An inter-laboratory comparison assessing the quality of seawater carbon dioxide measurements. *Marine Chemistry*, 171, 36–43. <https://doi.org/10.1016/j.marchem.2015.02.002>
- Buitenhuis, E. T., Hashioka, T., & Quércé, C. L. (2013). Combined constraints on global ocean primary production using observations and models. *Global Biogeochemical Cycles*, 27(3), 847–858. <https://doi.org/10.1002/gbc.20074>
- Chen, T., & Guestrin, C. (2016). Xgboost: A scalable tree boosting system. In *Proceedings of the 22nd acm sigkdd international conference on knowledge discovery and data mining* (pp. 785–794). <https://doi.org/10.1145/2939672.2939785>
- Conway, T. J., Tans, P. P., Waterman, L. S., Thoning, K. W., Kitzis, D. R., Masarie, K. A., & Zhang, N. (1994). Evidence for interannual variability of the carbon cycle from the national oceanic and atmospheric administration/climate monitoring and diagnostics laboratory global air sampling network. *Journal of Geophysical Research*, 99(D11), 22831–22855. <https://doi.org/10.1029/94jd01951>
- de Boyer Montégut, C., Madec, G., Fischer, A. S., Lazar, A., & Iudicone, D. (2004). Mixed layer depth over the global ocean: An examination of profile data and a profile-based climatology. *Journal of Geophysical Research*, 109(C12), C12003. <https://doi.org/10.1029/2004jc002378>

Acknowledgments

We acknowledge support from Columbia University and the National Oceanic and Atmospheric Administration (NOAA, agreement no. NA20OAR4310340). M. Y acknowledges support from the Data Science Institute scholar program. We thank the Global Carbon Project and the model developers for use of the Global Ocean Biochemical Models (GOBMs). SOCAT is an international effort, endorsed by the International Ocean Carbon Coordination Project (IOCCP), the Surface Ocean Lower Atmosphere Study (SOLAS) and the Integrated Marine Biosphere Research (IMBeR) program, to deliver a uniformly quality-controlled surface ocean CO_2 database. The many researchers and funding agencies responsible for the collection of data and quality control are thanked for their contributions to SOCAT. We acknowledge the ocean biogeochemical modelers who contribute to the Global Carbon Budget for sharing their output with us; and we thank Judith Hauck for her leadership on this effort.

- Denman, K. L., Brasseur, G. P., Chidthaisong, A., Ciais, P., Cox, P. M., Dickinson, R. E., & Steffen, W. (2007). Couplings between changes in the climate system and biogeochemistry. In *Climate change 2007: The physical science basis* (pp. 499–588). Cambridge University Press.
- Denvil-Sommer, A., Gehlen, M., Vrac, M., & Mejia, C. (2019). Lsce-ffnn-v1: A two-step neural network model for the reconstruction of Surface Ocean pCO₂ over the Global Ocean. *Geoscientific Model Development*, 12(5), 2091–2105. <https://doi.org/10.5194/gmd-12-2091-2019>
- Dickson, A. G., Sabine, C. L., & Christian, J. R. (2007). Guide to best practices for ocean CO₂ measurements. In *PICES Special Publication 3* (pp. 191).
- Doney, S. C., Lima, I., Feely, R. A., Glover, D. M., Lindsay, K., Mahowald, N., & Wanninkhof, R. (2009). Mechanisms governing interannual variability in upper-ocean inorganic carbon system and air–sea CO₂ fluxes: Physical climate and atmospheric dust. *Deep Sea Research Part II: Topical Studies in Oceanography*, 56(8–10), 640–655. <https://doi.org/10.1016/j.dsr2.2008.12.006>
- Dore, J. E., Lukas, R., Sadler, D. W., Church, M. J., & Karl, D. M. (2009). Physical and biogeochemical modulation of ocean acidification in the central north pacific. *Proceedings of the National Academy of Sciences*, 106(30), 12235–12240. <https://doi.org/10.1073/pnas.0906044106>
- Fay, A. R., Gregor, L., Landschützer, P., McKinley, G. A., Gruber, N., Gehlen, M., et al. (2021). Harmonization of global surface ocean pCO₂ mapped products and their flux calculations; an improved estimate of the ocean carbon sink. *Earth System Science Data Discussions*, 1–32. <https://doi.org/10.5194/essd-2021-16>
- Fay, A. R., & McKinley, G. A. (2013). Global trends in surface ocean pCO₂ from in situ data. *Global Biogeochemical Cycles*, 27, 541–557. <https://doi.org/10.1002/gbc.20051>
- Fay, A. R., & McKinley, G. A. (2017). Correlations of surface ocean pCO₂ to satellite chlorophyll on monthly to interannual timescales. *Global Biogeochemical Cycles*, 31(3), 436–455. <https://doi.org/10.1002/2016GB005563>
- Fay, A. R., & McKinley, G. A. (2021). Observed regional fluxes to constrain modeled estimates of the ocean carbon sink. *Geophysical Research Letters*, 48, e2021GL095325. <https://doi.org/10.1029/2021gl095325>
- Friedlingstein, P., Jones, M. W., O'Sullivan, M., Andrew, R. M., Hauck, J., Peters, G. P., et al. (2019). Global carbon budget 2019. *Earth System Science Data*, 11(4), 1783–1838. <https://doi.org/10.5194/essd-11-1783-2019>
- Friedlingstein, P., O'Sullivan, M., Jones, M. W., Andrew, R. M., Hauck, J., Olsen, A., et al. (2020). Global carbon budget 2020. *Earth System Science Data*, 12(4), 3269–3340.
- Gade, K. (2010). A non-singular horizontal position representation. *Journal of Navigation*, 63(3), 395–417. <https://doi.org/10.1017/s0373463309990415>
- Gloege, L., McKinley, G. A., Landschützer, P., Fay, A. R., Frölicher, T. L., et al. (2021). Quantifying errors in observationally based estimates of ocean carbon sink variability. *Global Biogeochemical Cycles*, 35(4), e2020GB006788. <https://doi.org/10.1029/2020gb006788>
- Good, S. A., Martin, M. J., & Rayner, N. A. (2013). En4: Quality controlled ocean temperature and salinity profiles and monthly objective analyses with uncertainty estimates. *Journal of Geophysical Research: Oceans*, 118(12), 6704–6716. <https://doi.org/10.1002/2013jc009067>
- Goodfellow, I., Bengio, Y., & Courville, A. (2016). *Deep learning*. MIT Press. Retrieved from <http://www.deeplearningbook.org>
- Gregor, L., & Gruber, N. (2021). OceanSODA-ETHZ: A global gridded data set of the Surface Ocean carbonate system for seasonal to decadal studies of ocean acidification. *Earth System Science Data*, 13, 777–808. <https://doi.org/10.5194/essd-13-777-2021>
- Gregor, L., Kok, S., & Monteiro, P. (2017). Empirical methods for the estimation of Southern Ocean CO₂: Support vector and random forest regression. *Biogeosciences*, 14(23), 5551–5569. <https://doi.org/10.5194/bg-14-5551-2017>
- Gregor, L., Lebehot, A. D., Kok, S., & Scheel Monteiro, P. M. (2019). A comparative assessment of the uncertainties of global surface ocean CO₂ estimates using a machine-learning ensemble (CSIR-ML6 version 2019a)—have we hit the wall? *Geoscientific Model Development*, 12(12), 5113–5136. <https://doi.org/10.5194/gmd-12-5113-2019>
- Gruber, N., Clement, D., Carter, B. R., Feely, R. A., Van Heuven, S., Hoppema, M., et al. (2019). The oceanic sink for anthropogenic CO₂ from 1994 to 2007. *Science*, 363(6432), 1193–1199. <https://doi.org/10.1126/science.aau5153>
- Gruber, N., Landschützer, P., & Lovenduski, N. S. (2019). The variable Southern Ocean carbon sink. *Annual Review of Marine Science*, 11, 159–186. <https://doi.org/10.1146/annurev-marine-121916-063407>
- Hain, M. P., Sigman, D. M., Higgins, J. A., & Haug, G. H. (2015). The effects of secular calcium and magnesium concentration changes on the thermodynamics of seawater acid/base chemistry: Implications for eocene and cretaceous ocean carbon chemistry and buffering. *Global Biogeochemical Cycles*, 29(5), 517–533. <https://doi.org/10.1002/2014gb004986>
- Harada, Y., Kamahori, H., Kobayashi, C., Endo, H., Kobayashi, S., Ota, Y., et al. (2016). The JRA-55 reanalysis: Representation of atmospheric circulation and climate variability. *Journal of the Meteorological Society of Japan. Series II*, 94(3), 269–302. <https://doi.org/10.2151/jmsj.2016-015>
- Hauck, J., Zeising, M., Le Quéré, C., Gruber, N., Bakker, D. C. E., Bopp, L., & Séférian, R. (2020). Consistency and challenges in the ocean carbon sink estimate for the Global Carbon Budget. *Frontiers in Marine Science*, 7, 3167. <https://doi.org/10.3389/fmars.2020.571720>
- Hersbach, H., Bell, B., Berrisford, P., Hirahara, S., Horányi, A., Muñoz-Sabater, J., et al. (2020). The ERA5 global reanalysis. *Quarterly Journal of the Royal Meteorological Society*, 146(730), 1999–2049. <https://doi.org/10.1002/qj.3803>
- Jacobson, A. R., Mikaloff Fletcher, S. E., Gruber, N., Sarmiento, J. L., & Gloor, M. (2007). A joint atmosphere–ocean inversion for surface fluxes of carbon dioxide: 1. Methods and global-scale fluxes. *Global Biogeochemical Cycles*, 21(1), 273. <https://doi.org/10.1029/2005gb002556>
- Karpatne, A., Watkins, W., Read, J., & Kumar, V. (2017). *Physics-guided neural networks (pgnn): An application in lake temperature modeling*. arXiv preprint arXiv:1710.11431.
- Lacroix, F., Ilyina, T., & Hartmann, J. (2020). Oceanic CO₂ outgassing and biological production hotspots induced by pre-industrial river loads of nutrients and carbon in a global modeling approach. *Biogeosciences*, 17(1), 55–88. <https://doi.org/10.5194/bg-17-55-2020>
- Landschützer, P., Gruber, N., Bakker, D., & Schuster, U. (2014). Recent variability of the global ocean carbon sink. *Global Biogeochemical Cycles*, 28(9), 927–949. <https://doi.org/10.1002/2014gb004853>
- Landschützer, P., Gruber, N., & Bakker, D. C. (2016). Decadal variations and trends of the global ocean carbon sink. *Global Biogeochemical Cycles*, 30(10), 1396–1417. <https://doi.org/10.1002/2015gb005359>
- Landschützer, P., Gruber, N., & Bakker, D. C. (2020). *An observation-based global monthly gridded sea surface pCO₂ product from 1982 onward and its monthly climatology (NCEI Accession 0160558)*. Version 5.5. NOAA National Centers for Environmental Information. <https://doi.org/10.7289/V5Z899N6>
- Landschützer, P., Laruelle, G. G., Roobaert, A., & Regnier, P. (2020). A uniform pCO₂ climatology combining open and coastal oceans. *Earth System Science Data*, 1–30.
- Law, R. M., Ziehn, T., Matear, R. J., Lenton, A., Chamberlain, M. A., Stevens, L. E., et al. (2017). The carbon cycle in the Australian community climate and earth system simulator (access-esm1)—part 1: Model description and pre-industrial simulation. *Geoscientific Model Development*, 10(7), 2567–2590. <https://doi.org/10.5194/gmd-10-2567-2017>
- Le Quéré, C., Raupach, M. R., Canadell, J. G., Marland, G., Bopp, L., Ciais, P., et al. (2009). Trends in the sources and sinks of carbon dioxide. *Nature Geoscience*, 2(12), 831–836. <https://doi.org/10.1038/ngeo0689>

- Lueker, T. J., Dickson, A. G., & Keeling, C. D. (2000). Ocean pCO₂ calculated from dissolved inorganic carbon, alkalinity, and equations for k₁ and k₂: Validation based on laboratory measurements of CO₂ in gas and seawater at equilibrium. *Marine Chemistry*, 70(1–3), 105–119. [https://doi.org/10.1016/S0304-4203\(00\)00022-0](https://doi.org/10.1016/S0304-4203(00)00022-0)
- Maritorena, S., d'Andon, O. H. F., Mangin, A., & Siegel, D. A. (2010). Merged satellite ocean color data products using a bio-optical model: Characteristics, benefits and issues. *Remote Sensing of Environment*, 114(8), 1791–1804. <https://doi.org/10.1016/j.rse.2010.04.002>
- McKinley, G. A., Fay, A. R., Eddebar, Y. A., Gloege, L., & Lovenduski, N. S. (2020). External forcing explains recent decadal variability of the ocean carbon sink. *AGU Advances*, 1(2), e2019AV000149. <https://doi.org/10.1029/2019av000149>
- McKinley, G. A., Pilcher, D. J., Fay, A. R., Lindsay, K., Long, M. C., & Lovenduski, N. S. (2016). Timescales for detection of trends in the ocean carbon sink. *Nature*, 530(7591), 469–472. <https://doi.org/10.1038/nature16958>
- Mears, C. A., Scott, J., Wentz, F. J., Ricciardulli, L., Leidner, S. M., Hoffman, R., & Atlas, R. (2019). A near-real-time version of the cross-calibrated multiplatform (ccmp) ocean surface wind velocity data set. *Journal of Geophysical Research: Oceans*, 124(10), 6997–7010. <https://doi.org/10.1029/2019jc015367>
- Olsen, A., Lange, N., Key, R. M., Tanhua, T., Álvarez, M., Becker, S., et al. (2019). Glodapv2. 2019—an update of glodapv2. *Earth System Science Data*, 11(3), 1437–1461. <https://doi.org/10.5194/essd-11-1437-2019>
- Orr, J. C., Najjar, R. G., Aumont, O., Bopp, L., Bullister, J. L., Danabasoglu, G., et al. (2017). Biogeochemical protocols and diagnostics for the cmip6 ocean model intercomparison project (omip). *Geoscientific Model Development*, 10(6), 2169–2199. <https://doi.org/10.5194/gmd-10-2169-2017>
- Paulsen, H., Ilyina, T., Six, K. D., & Stemmler, I. (2017). Incorporating a prognostic representation of marine nitrogen fixers into the global ocean biogeochemical model hamocc. *Journal of Advances in Modeling Earth Systems*, 9(1), 438–464. <https://doi.org/10.1002/2016ms000737>
- Peters, G. P., Le Quéré, C., Andrew, R. M., Canadell, J. G., Friedlingstein, P., Ilyina, T., et al. (2017). Towards real-time verification of CO₂ emissions. *Nature Climate Change*, 7(12), 848–850. <https://doi.org/10.1038/s41558-017-0013-9>
- Raupach, M. R., Gloor, M., Sarmiento, J. L., Canadell, J. G., Frolicher, T. L., Gasser, T., et al. (2014). The declining uptake rate of atmospheric CO₂ by land and ocean sinks. *Biogeosciences*, 11(13), 3453–3475. <https://doi.org/10.5194/bg-11-3453-2014>
- Reichstein, M., Camps-Valls, G., Stevens, B., Jung, M., Denzler, J., Carvalhais, N., & Prabhat (2019). Deep learning and process understanding for data-driven earth system science. *Nature*, 566(7743), 195–204. <https://doi.org/10.1038/s41586-019-0912-1>
- Resplandy, L., Keeling, R., Rödenbeck, C., Stephens, B., Khattiwala, S., Rodgers, K., et al. (2018). Revision of global carbon fluxes based on a reassessment of oceanic and riverine carbon transport. *Nature Geoscience*, 11(7), 504–509. <https://doi.org/10.1038/s41561-018-0151-3>
- Reynolds, R. W., Rayner, N. A., Smith, T. M., Stokes, D. C., & Wang, W. (2002). An improved in situ and satellite SST analysis for climate. *Journal of Climate*, 15(13), 1609–1625. [https://doi.org/10.1175/1520-0442\(2002\)015<1609:aissas>2.0.co;2](https://doi.org/10.1175/1520-0442(2002)015<1609:aissas>2.0.co;2)
- Ridge, S., & McKinley, G. A. (2020). Ocean carbon uptake under aggressive emission mitigation. *Biogeosciences Discussions*. <https://doi.org/10.5194/bg-2020-254>
- Rödenbeck, C., Bakker, D., Metzl, N., Olsen, A., Sabine, C., Cassar, N., et al. (2014). Interannual sea–air CO₂ flux variability from an observation-driven ocean mixed-layer scheme. *Biogeosciences*, 11(17), 4599–4613. <https://doi.org/10.5194/bg-11-4599-2014>
- Rödenbeck, C., Bakker, D. C., Gruber, N., Iida, Y., Jacobson, A. R., Jones, S., et al. (2015). Data-based estimates of the ocean carbon sink variability—first results of the surface ocean pCO₂ mapping intercomparison (socom). *Biogeosciences*, 12, 7251–7278. <https://doi.org/10.5194/bg-12-7251-2015>
- Roobaert, A., Laruelle, G. G., Landschützer, P., Gruber, N., Chou, L., & Regnier, P. (2019). The spatiotemporal dynamics of the sources and sinks of CO₂ in the global coastal ocean. *Global Biogeochemical Cycles*, 33(12), 1693–1714. <https://doi.org/10.1029/2019gb006239>
- Sabine, C. L., Hankin, S., Koyuk, H., Bakker, D. C. E., Pfeil, B., Olsen, A., et al. (2013). Surface ocean CO₂ atlas (socat) gridded data products. *Earth System Science Data*, 5(1), 145–153. <https://doi.org/10.5194/essd-5-145-2013>
- Sasse, T., McNeil, B., & Abramowitz, G. (2013). A novel method for diagnosing seasonal to inter-annual surface ocean carbon dynamics from bottle data using neural networks. *Biogeosciences*, 10(6), 4319–4340. <https://doi.org/10.5194/bg-10-4319-2013>
- Schwinger, J., Goris, N., Tjiputra, J. F., Kriest, I., Bentsen, M., Bethke, I., et al. (2016). Evaluation of noresm-oc (versions 1 and 1.2), the ocean carbon-cycle stand-alone configuration of the Norwegian earth system model (noresm1). *Geoscientific Model Development*, 9, 2589–2622. <https://doi.org/10.5194/gmd-9-2589-2016>
- Stamell, J., Rustagi, R. R., Gloege, L., & McKinley, G. A. (2020). Strengths and weaknesses of three machine learning methods for pCO₂ interpolation. *Geoscientific Model Development Discussions*, 1–25
- Stow, C. A., Jolliff, J., McGillicuddy, D. J., Jr, Doney, S. C., Allen, J. I., Friedrichs, M. A., & Wallhead, P. (2009). Skill assessment for coupled biological/physical models of marine systems. *Journal of Marine Systems*, 76(1–2), 4–15. <https://doi.org/10.1016/j.jmarsys.2008.03.011>
- Sulpis, O., Lauvset, S. K., & Hagens, M. (2020). Current estimates of k₁* and k₂* appear inconsistent with measured CO₂ system parameters in cold oceanic regions. *Ocean Science*, 16(4), 847–862. <https://doi.org/10.5194/os-16-847-2020>
- Sweeney, C., Gloor, E., Jacobson, A. R., Key, R. M., McKinley, G., Sarmiento, J. L., & Wanninkhof, R. (2007). Constraining global air-sea gas exchange for CO₂ with recent bomb 14c measurements. *Global Biogeochemical Cycles*, 21(2), GB2015. <https://doi.org/10.1029/2006gb002784>
- Takahashi, T., Sutherland, S. C., & Kozyr, A. (2019). *Global ocean surface water partial pressure of CO₂ database: Measurements performed during 1957–2018*. (version 2018).
- Taylor, K. E. (2001). Summarizing multiple aspects of model performance in a single diagram. *Journal of Geophysical Research*, 106(D7), 7183–7192. <https://doi.org/10.1029/2000jd900719>
- Tjiputra, J. F., Olsen, A., Bopp, L., Lenton, A., Pfeil, B., Roy, T., et al. (2014). Long-term surface pCO₂ trends from observations and models. *Tellus B: Chemical and Physical Meteorology*, 66(1), 23083. <https://doi.org/10.3402/tellusb.v66.23083>
- Wanninkhof, R. (1992). Relationship between wind speed and gas exchange over the ocean. *Journal of Geophysical Research*, 97(C5), 7373–7382. <https://doi.org/10.1029/92jc00188>
- Wanninkhof, R. (2014). Relationship between wind speed and gas exchange over the ocean revisited. *Limnology and Oceanography: Methods*, 12(6), 351–362. <https://doi.org/10.4319/lom.2014.12.351>
- Watt-Meyer, O., Brenowitz, N. D., Clark, S. K., Henn, B., Kwa, A., McGibbon, J., et al. (2021). Correcting weather and climate models by machine learning nudged historical simulations. *Geophysical Research Letters*, 48(15), e2021GL092555. <https://doi.org/10.1002/essoar.10505959.1>
- Weiss, R. (1974). Carbon dioxide in water and seawater: The solubility of a non-ideal gas. *Marine Chemistry*, 2(3), 203–215.